

## Coarse- versus fine-grain quartz OSL and cosmogenic $^{10}\text{Be}$ dating of deformed fluvial terraces on the northeast Pamir margin, northwest China

Jessica A. Thompson<sup>a,b,\*</sup>, Jie Chen<sup>a</sup>, Huili Yang<sup>a</sup>, Tao Li<sup>c</sup>, Bodo Bookhagen<sup>d,1</sup>, Douglas Burbank<sup>b</sup>

<sup>a</sup> State Key Laboratory of Earthquake Dynamics, Institute of Geology, China Earthquake Administration, Beijing, China

<sup>b</sup> Department of Earth Science, University of California Santa Barbara, Santa Barbara, CA, 93106, USA

<sup>c</sup> Guangdong Provincial Key Lab of Geodynamics and Geohazards, School of Earth Sciences and Engineering, Sun Yat-Sen University, Guangzhou, China

<sup>d</sup> Department of Geography, University of California Santa Barbara, Santa Barbara, CA, 93106, USA



### ARTICLE INFO

#### Keywords:

Tectonic geomorphology  
Deformation  
Quaternary terraces  
Pamir  
Tian shan

### ABSTRACT

Along the NE Pamir margin, flights of late Quaternary fluvial terraces span actively deforming fault-related folds. We present detailed results on two terraces dated using optically stimulated luminescence (OSL) and cosmogenic radionuclide  $^{10}\text{Be}$  (CRN) techniques. Quartz OSL dating of two different grain sizes (4–11  $\mu\text{m}$  and 90–180  $\mu\text{m}$ ) revealed the fine-grain quartz fraction may overestimate the terrace ages by up to a factor of ten. Two-mm, small-aliquot, coarse-grain quartz OSL ages, calculated using the minimum age model, yielded stratigraphically consistent ages within error and dated times of terrace deposition to  $\sim 9$  and  $\sim 16$  ka. We speculate that, in this arid environment, fine-grain samples can be transported and deposited in single, turbid, and (sometimes) nighttime floods that prevent thorough bleaching and, thereby, can lead to relatively large residual OSL signals. In contrast, sand in the fluvial system is likely to have a much longer residence time during transport, thereby providing greater opportunities for thorough bleaching. CRN  $^{10}\text{Be}$  depth profiles date the timing of terrace abandonment to  $\sim 8$  and  $\sim 14$  ka: ages that generally agree with the coarse-grain quartz OSL ages. Our new terrace age of  $\sim 13$ – $14$  ka is broadly consistent with other terraces in the region that indicate terrace deposition and subsequent abandonment occurred primarily during glacial-interglacial transitions, thereby suggesting a climatic control on the formation of these terraces on the margins of the Tarim Basin. Furthermore, tectonic shortening rates calculated from these deformed terraces range from  $\sim 1.2$  to  $\sim 4.6$  mm/a and, when combined with shortening rates from other structures in the region, illuminate the late Quaternary basinward migration of deformation to faults and folds along the Pamir-Tian Shan collisional interface.

### 1. Introduction

Fluvial terraces can be excellent geomorphic markers that record recent tectonic deformation and uplift, in addition to capturing a landscape's response to climatic events, e.g., Repka et al. (1997); Pan et al. (2003); and Burbank and Anderson (2011). Fluvial terraces may form in response to changes in deformation, e.g., uplift rates, or climate, e.g., sediment supply or discharge, allowing a river to incise into fill or bedrock, thereby abandoning the previous riverbed. Whereas the original terrace surface mimics the gradient of the previous riverbed, it can be subsequently deformed by faults and folds. The deviation from the original terrace gradient can then be used to calculate deformation rates, if the terrace can be accurately dated. Thus, reliable dating of fluvial terraces is a key step to unraveling the geomorphic record and characterizing deformation rates. Dating has proven challenging in

semi-arid to arid settings, where readily dateable materials, such as organic debris for  $^{14}\text{C}$  dating, are uncommon. Recent advances in cosmogenic radionuclide (CRN), e.g., Gosse and Phillips (2001), and optically stimulated luminescence (OSL) dating (Aitken, 1998) have allowed successful dating of terrace surfaces in these settings, e.g., Rittenour (2008); Porat et al. (2009); Guralnik et al. (2011); Viveen et al. (2012); and Li et al. (2013). Given uncertainties associated with individual dating methods, dating of terraces using both cosmogenic  $^{10}\text{Be}$  and OSL techniques has become increasingly common (Hetzel et al., 2004; Owen et al., 2006; DeLong and Arnold, 2007; Nissen et al., 2009; Fruchter et al., 2011; Owen et al., 2011; Guralnik et al., 2011; Lee et al., 2011; Viveen et al., 2012). Importantly, OSL and  $^{10}\text{Be}$  date different geomorphic events: OSL dates the deposition of the sediments that aggrade above a strath, whereas cosmogenic  $^{10}\text{Be}$  dates the abandonment and stabilization of the terrace surface. Thus, when combined

\* Corresponding author. Institute of Tectonic Studies, University of Texas El Paso, 500 West University Ave, El Paso, Texas, 79902, USA .

E-mail address: [jajobe@utep.edu](mailto:jajobe@utep.edu) (J.A. Thompson).

<sup>1</sup> Now at: Institute of Earth and Environmental Sciences, University of Potsdam, 14476 Potsdam, Germany.

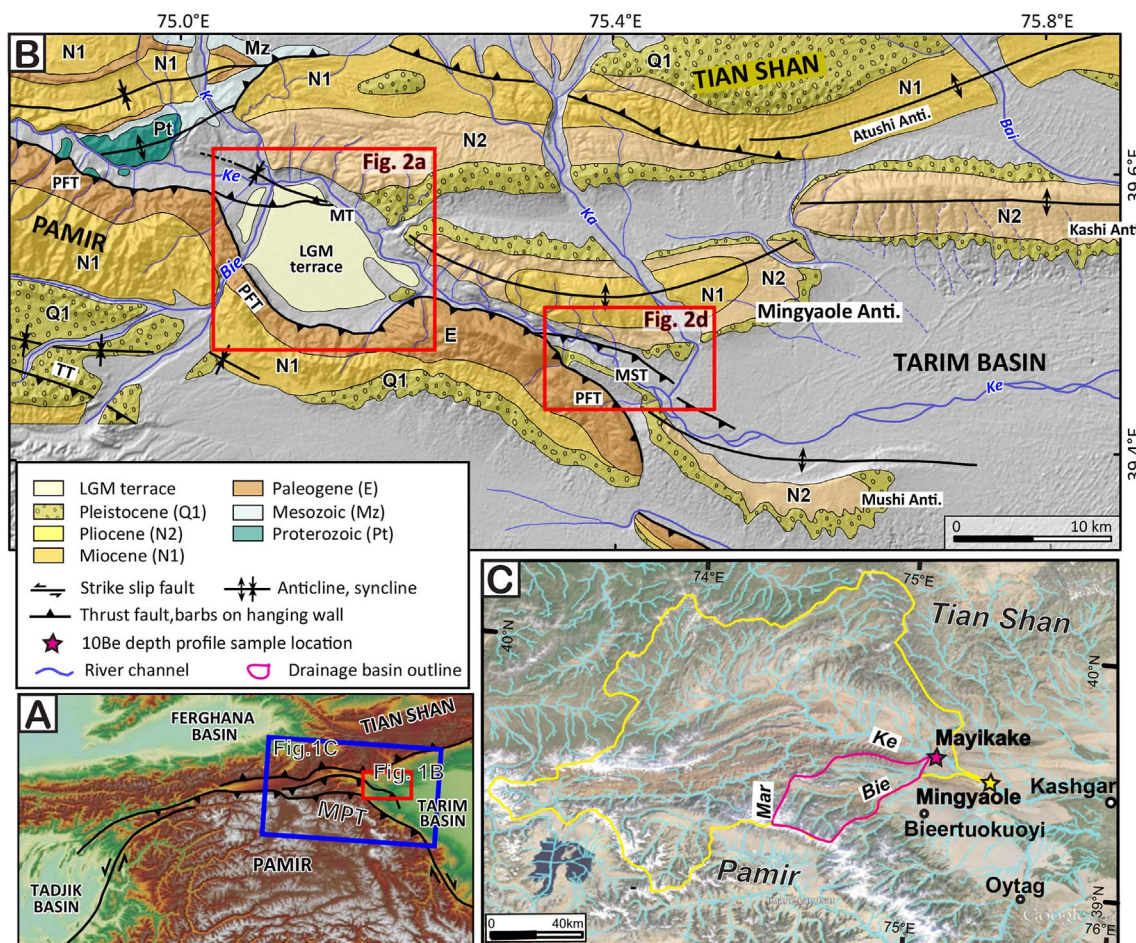


Fig. 1. (A) Topography of the Pamir and surrounding area. (B) Simplified geologic map of the western Tarim Basin. Faults: MPT – Main Pamir Thrust, MST – Mingyaole South Thrust, MT – Mayikake Thrust, PFT – Pamir Frontal Thrust, TT – Takegai Thrust. Rivers: Bie – Bieertuokuoyi River, K – Kangsu River, Ka – Kalangoulke River, Ke – Kezilezu River, Mar – Markansu River. (C) GoogleEarth image showing regional river system, <sup>10</sup>Be depth profile sample locations, and their respective upstream catchments.

with additional field data and observations, the difference between cosmogenic <sup>10</sup>Be- and OSL-derived ages may reveal important information about the geomorphic system and the formation of the terrace surfaces (Guralnik et al., 2011), such as the terrace aggradation rates, uplift and incision rates, and paleo-erosion rates.

Flights of fluvial terraces span large areas of the Pamir and Tian Shan foreland basins in the western Tarim Basin in northwest China (Fig. 1) (Bufe et al., 2016). Many of these terraces are deformed by active faults and folds and record the late Quaternary deformation of these structures (Scharer et al., 2006; Heermance et al., 2008; Li et al., 2012, 2017, 2013, 2015a, 2015b; Thompson Jobe et al., 2017). Deformation by numerous active structures in this area inhibits reliable correlation of undated fluvial terraces for calculating slip rates on faults and folds. Hence, to determine local deformation rates, terraces crossing each individual structure must be dated. Previously, several deformed terraces have been dated using fine-grain quartz OSL (Li et al., 2012, 2013; Thompson Jobe et al., 2017). Given that numerous younger terraces yielded ages similar to older, higher surfaces dated using the same grain size and protocol, we suspect that many of these samples from younger terraces may have been poorly bleached, resulting in ages that overestimate the actual depositional ages. To test this possibility, we compared both fine- and coarse-grain quartz OSL dating techniques for consistency with each other and with independent ages from cosmogenic <sup>10</sup>Be depth profiles.

Here, we present a case study of two fluvial terraces in the western Tarim Basin, focusing on (i) the applicability of quartz OSL and cosmogenic <sup>10</sup>Be dating techniques to date fluvial terraces in an arid,

tectonically active region of NW China; (ii) assessment of which grain sizes are most appropriate for both OSL and cosmogenic <sup>10</sup>Be dating; (iii) evaluation of which OSL age model is most appropriate for determining a reliable depositional age for these terraces and (iv) calculation of deformation rates on three active structures that deform these two terraces. Ultimately, our goal is to develop a regional chronology of the widespread terraces to assess slip rates and climate-tectonic interactions across the NE margin of the Pamir orogen. This study presents a subset of our data toward that end.

## 2. Regional setting

In NW China, the western Tarim Basin lies between the Pamir and Tian Shan at the northwestern end of the Himalayan-Tibetan orogen, which formed as a result of the Indo-Eurasian collision (Fig. 1). In the western Tarim Basin, numerous Miocene-to-Recent faults and folds deform the Cenozoic sedimentary basin fill along the margins of the basin (Chen et al., 2002; Scharer et al., 2006; Heermance et al., 2008; Thompson et al., 2015). The basin-bounding faults have also uplifted and exposed Mesozoic and Paleozoic sedimentary and metamorphic units that have served as source areas for Quaternary sediment within the Pamir and Tian Shan orogens (Sobel et al., 2013).

The Main Pamir Thrust, defining the northern margin of the Pamir Plateau, initiated approximately 20 Ma (Sobel and Dumitru, 1997), and deformation propagated basinward during the Late Miocene to form the Takegai and Pamir Frontal Thrusts (Thompson et al., 2015). During the Quaternary, deformation has been accommodated on the Pamir

Frontal, Takegai, and Main Pamir Thrusts along the margins of the Tarim Basin, although in the last 125 ka, most deformation has been focused along a narrow corridor between the Pamir and Tian Shan (Li et al., 2012, 2015b; Thompson Jobe et al., 2017). Since ~0.35 Ma, the Pamir Frontal Thrust has maintained a nearly uniform shortening rate of 6–8 mm/a (Li et al., 2012).

The Kezilesu River (Fig. 1B and C) is the largest river in the region, currently trapped between the Pamir and Tian Shan and flowing eastward parallel to the regional structural trend. In the western Tarim Basin, all major tributaries flow either north from the Pamir or south from the Tian Shan and join the Kezilesu River (Fig. 1B and C). In the Tian Shan, the bedrock in the source area comprises older formations of carbonates, clastics, and some igneous rocks. In the Pamir, igneous and clastic units dominate the source area. The western Tarim Basin has a present-day arid to semi-arid climate with highly seasonal variations in precipitation, which influence fluvial discharge dynamics. Driven by snowmelt, intense storms, and cloudbursts, the highest flows occur in the spring and summer, whereas slower flows occur in the winter. These variations in seasonal discharge have implications for the transport of sediment through the fluvial system, i.e., flash floods, transient storage in overbank deposits, or on bars in between high discharge flows, and they affect the bleaching of grains used in OSL dating and the deposition of sediment on the landscape. Within the foreland, most rivers have beveled the underlying Tertiary strata and created suites of gravel-covered strath terraces during the late Quaternary (Scharer et al., 2006; Heermance et al., 2008; Li et al., 2012, 2013, 2015a, 2015b; Bufer et al., 2016, 2017; Thompson Jobe et al., 2017).

We selected two representative sites on fluvial terraces along the Pamir Frontal Thrust on the NE Pamir margin in the western Tarim Basin (Fig. 1 and Fig. 2), and sampled the sand-and-gravel cover above

the bedrock strath. At each site, we collected four OSL samples and one cosmogenic <sup>10</sup>Be depth profile of both sand and pebbles, resulting in a total of 8 OSL samples and 2 cosmogenic <sup>10</sup>Be depth profiles that comprise 12 sand samples and 4 pebble samples.

### 3. Study area

#### 3.1. Mayikake

The Mayikake site sits within a large, flat aggradation surface, 15 by 10 km, near the village of Mayikake (Fig. 1B and Fig. 2A). The extensive terrace surface is bounded on its northern side by the Kezilesu River and on the other margins by Cenozoic bedrock, exposed by uplift on the Pamir Frontal Thrust (PFT). On the SW margin, the terrace surface is cut by the Biertuokuoyi Frontal Thrust, a segment of the PFT (Fig. 2A). This fault offsets both Holocene alluvial fans at the mountain front and river terraces formed by the Biertuokuoyi River. SW-dipping Paleogene sediments were thrust over the fluvial terrace deposits along a fault dipping  $75 \pm 5^\circ$  SW. Striae on the surface of the fault plane have a rake of  $34^\circ$ , indicating a strike-slip to dip-slip ratio of ~3:2 (Li et al., 2012). Differential GPS surveys of the terrace surface offset by the Biertuokuoyi Frontal Thrust indicate a vertical separation of ~38 m (Li et al., 2012). On the northern part of the terrace, the Mayikake Thrust, a gently, north-dipping fault, cuts the surface to produce a fault scarp that extends no longer than ~8 km and is ~15 m high (Li et al., 2012). Recent incision of the terrace surface crossing the fault plane reveals a dip of ~16° (Li et al., 2012).

Fluvial terrace gravels, ranging from 2- to > 10-m thick, cap a strath eroded into lithified Cenozoic units. Since abandonment of the terrace surface, the river has incised between 20 and 70 m into the underlying

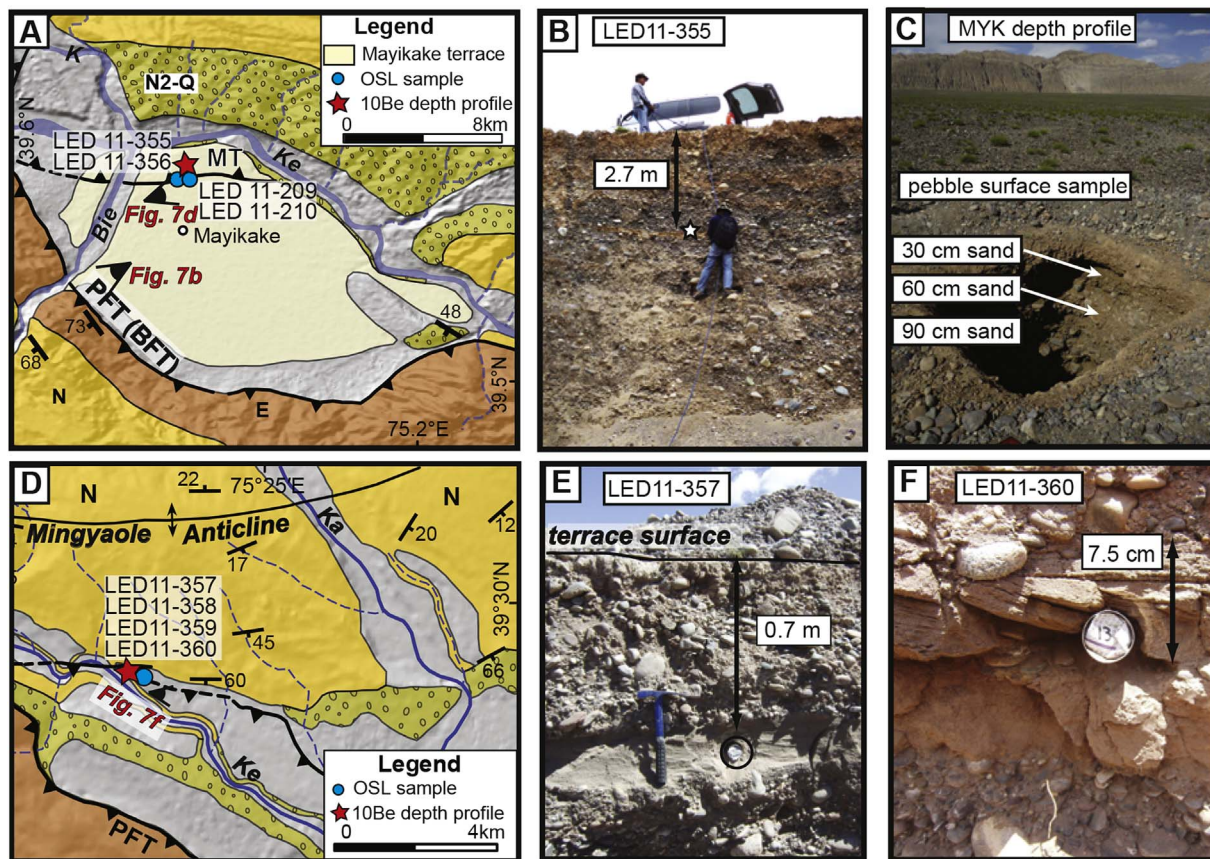


Fig. 2. (A) Simplified geologic map of the Mayikake basin (location in Fig. 1B). (B) Sample LED 11-355 (C) <sup>10</sup>Be depth profile on Mayikake terrace surface (D) Simplified geologic map of the southern Mingyaole anticline (D) Sample LED 11-357 (F) Sample LED 11-360. BFT – Biertuokuoyi Frontal Thrust, MT – Mayikake Thrust, PFT – Pamir Frontal Thrust, N – Neogene, E – Paleogene, N2-Q – Miocene-Pleistocene conglomerates. Rivers: Bie – Biertuokuoyi River, K – Kangsu River, Ka – Kalangoulke River, Ke – Kezilesu River.

**Table 1**  
Location and lithology of OSL samples.

Sample No.	Latitude/Longitude	Elevation (m)	Terrace Level	Lithology	Depth (m)	Thickness of silt lens (cm) <sup>a</sup>
<b>Mayikake</b>						
LED11-210	39.5811°N/75.0957°E	1869	T2	muddy silt	1.9	8
LED11-209	39.5811°N/75.0957°E	1869	T2	muddy silt	2.2	15
LED11-355	39.5833°N/75.1043°E	1869	T2	silty fine sand	2.7	8
LED11-356	39.5833°N/75.1043°E	1869	T2	muddy silt	3.1	8
<b>Mingyaole</b>						
LED11-360	39.4835°N/75.3822°E	1670	T2	fine sand	0.6	8
LED11-357	39.4836°N/75.3821°E	1670	T2	silty fine sand	0.7	30
LED11-359	39.4835°N/75.3822°E	1670	T2	sandy silt	0.8	45
LED11-358	39.4836°N/75.3821°E	1670	T2	sandy silt	1.0	25

<sup>a</sup> The thickness of the lens from which sample was collected, centered on the depth of the sample.

bedrock. The terrace surface displays a poorly-to-moderately developed desert pavement, with fractured and highly weathered clasts. Imbricated pebble-cobble clasts, with uncommon interbedded laminated and cross-bedded sands and silts, compose the gravel cover. We collected four OSL samples from trenches on the hanging wall of the Mayikake Thrust. All samples were collected from 8- to 15-cm-thick, muddy silt and sandy silt lenses from depths of 1.9–3.1 m (Fig. 2B, Table 1). Although the sampling site is near a fault, we carefully selected sites within the hanging wall of the fault where the primary stratigraphy was preserved, such that we are confident that fault-related deposits, such as colluvial wedges or ponding against the fault scarp, were excluded. The cosmogenic <sup>10</sup>Be depth profile was collected from a separate, hand-dug pit located ~40 m to the north of the fault scarp, where the surface had not been recently modified (Fig. 2C). Observations from the depth profile pit indicate no evidence of buried soils, depositional hiatuses, or extensive bioturbation.

Previous fine-grain quartz OSL dating of this terrace yielded an age of  $18.4 \pm 4.3$  ka ( $2\sigma$ ): an age correlated to a regional terrace level dated to the Last Glacial Maximum (LGM) (Li et al., 2012). This age, combined with the measured offsets, defined slip rates of ~3.6 and ~3.1 mm/a for the Pamir Frontal Thrust (Bieertuokuoyi Frontal Thrust in Li et al., 2012) and the Mayikake Thrust, respectively.

### 3.2. Mingyaole

The second site is a fluvial terrace on the southern side of the growing Mingyaole fold, adjacent to the Kezilesu River (Fig. 2D). The Mingyaole anticline initiated ~1.6 Ma (Chen et al., 2005; Thompson, 2013), and has accommodated ~1.5 km of shortening at a mean rate of ~0.9 mm/a (Chen et al., 2005). As the anticline continued to grow, terrace surfaces on the flanks of the anticline have been deformed to produce a series of fold scarps and flexural-slip fault scarps (Chen et al., 2005, 2007; Li et al., 2015a, b). We sampled from the upper tread of the fold scarp on the T2 terrace. The fold scarp on the T2 surface is ~16 m high and dips ~25° to the south. The cumulative shortening absorbed by the fold scarp is  $10.1^{+1.9}_{-1.6}$  m since the abandonment of the terrace surface (Li et al., 2015b). Despite the proximity to these tectonic features, intact sedimentary structures and field observations suggest a stratigraphy that is undisturbed by tectonic deformation.

Fluvial gravels ~5 m thick rest above a strath terrace that was beveled into Neogene sedimentary formations. Currently, the river flows ~60 m below the terrace surface and has incised through the terrace fill and underlying Neogene bedrock. The terrace surface has a poorly-to-moderately developed desert pavement, with fractured, weathered, and varnished clasts. The terrace deposits consist mostly of imbricated pebble-cobble clasts, with interbedded laminated and cross-bedded silty-sand lenses and uncommon massive, muddy silt beds ~10-cm thick (Fig. 2E and F). (See Li et al. (2015a) for a detailed description and geomorphic map of the terraces near Mingyaole.) We exploited man-made pits that were hand-dug ~2.5 m into the terrace surface.

Because the pits were not present when we previously visited this site in 2010 (samples were collected in 2011), we know the pits were dug less than a year before we sampled from them. We collected two OSL samples from each of two pits and the <sup>10</sup>Be depth profile from a third pit: all less than ~50 m apart. All OSL samples were collected from 7.5- to 45-cm-thick silty sand lenses from depths of 0.6–1 m (Fig. 2, Table 1). Observations from the depth-profile pit show no evidence of buried soils, depositional hiatuses, or extensive bioturbation. This terrace surface has not been previously dated, and our previous work suggested it might be equivalent to the LGM terrace at Mayikake based on surface characteristics.

## 4. OSL dating

OSL dating relies on the assumption that grains must be exposed to light for a certain length of time to remove the previous luminescence signal (Aitken, 1998). With insufficient exposure, grains remain incompletely bleached and retain a residual equivalent dose. Several factors affect the probability of bleaching sediments during fluvial transport, such as grain size (e.g., Stokes et al., 2001), turbidity (e.g., Berger and Luternauer, 1987), sediment load, water depth (e.g., Berger, 1990), sediment-transport distance (e.g., Stokes et al., 2001), and time in the fluvial system (Rittenour, 2008; Rhodes, 2011; ). Recent modeling and dating research suggest the opportunities for bleaching of the grains are largely related to the mode of transport through the fluvial system (Rittenour, 2008; Gray and Mahan, 2014; Cunningham et al., 2015). Because hydraulic conditions dictate that grains of different sizes will commonly have contrasting transport histories and may end up in different fluvial deposits, grains of different sizes are likely to have experienced different bleaching histories (Stokes et al., 2001; Rittenour, 2008). Beyond the tectonic implications, one goal of our research was to test the consistency of OSL dates from fine- and coarse-grain deposits in this arid setting.

### 4.1. OSL sample collection and analysis

We collected samples by hammering a metal tube parallel into the sediment layers. After removal from the surrounding sediment, we sealed the samples at both ends to prevent water loss and exposure to light during transport. The metal tubes were opened and the samples were processed under subdued red light at the Research Laboratory of Luminescence Dating at the Institute of Geology, China Earthquake Administration, in Beijing. All grain-size fractions were pretreated with 30% H<sub>2</sub>O<sub>2</sub> and 30% HCl to remove organics and carbonates, respectively. The fine-grain fraction (4–11 μm) was separated using Stokes' Law. The polymineralic fine-silt grains were immersed in hydrofluosilicic acid (40%) for three days in a centrifuge tube to isolate the quartz. The fine quartz grains were mounted on 9.7-mm steel discs from suspension in acetone. Coarse-grain samples (90–180 μm) were immersed in a 10% HF solution for 10 min, followed by a 40% HF bath for

40 min, then by 30% HCl for 40 min. The coarse-grain quartz grains were mounted on 9.7-mm steel discs using silicone gel to create small aliquots (~2-mm mask diameter). The purity of the quartz was checked by IR stimulation and verified through observation of background IR signal and the typical 110° TL peak. Nevertheless, we performed an OSL-IR depletion test (Duller, 2003) on every coarse-grain aliquot.

#### 4.2. OSL equipment and measurements

All fine-grain quartz samples, as well as coarse-grain quartz samples LED 11–210, LED 11–355, and LED 11–356, were measured using a Daybreak 2200 automated OSL reader, equipped with a combined blue ( $470 \pm 5$  nm) and infrared ( $880 \pm 80$  nm) LED OSL unit with a calibrated  $^{90}\text{Sr}/^{90}\text{Y}$  beta-radiation source (dose rate: 0.0327 Gy/s). Detection of the signal was through a 7-mm-thick U-340 glass filter. The coarse-grain samples LED 11–360 and LED 11–357, and additional LED 11–356 aliquots, in addition to preheat plateau and dose-recovery tests (Wintle and Murray, 2006) on sample LED 11–210, were measured using a Riso Reader model TL/OSL-DA-20 equipped with a calibrated  $^{90}\text{Sr}/^{90}\text{Y}$  beta-radiation sources (dose rate: 0.1051 Gy/s), blue ( $470 \pm 30$  nm;  $\sim 50$  mW/cm<sup>2</sup>) and infrared (IR: 880 nm  $\pm$  80 nm,  $\sim 145$  mW/cm<sup>2</sup>) LEDs, and detection through a 7-mm-thick U-340 glass filter (Botter-Jensen et al., 2000). We conducted quality tests to ensure both OSL readers were returning comparable results and checked against independent <sup>14</sup>C dating results (Liu et al., 2010). We are convinced that using two different readers has not introduced any additional uncertainties beyond the uncertainties in the equivalent dose, hereafter noted by  $D_e$ . All luminescence measurements were made at 125 °C to prevent re-trapping in the 110 °C TL trap with both IR- and blue-light stimulation power at 80%. All  $D_e$  measurements were made using the sensitivity-corrected, multiple aliquot regenerative (SMAR) protocol for silt-sized quartz (Lu et al., 2007; Table S1), or a modified, single-aliquot regenerative (SAR) protocol for fine-sand quartz (Murray and Wintle, 2000; Table S2), with a thermal wash at 280 °C at the end of each cycle. On one sample, LED 11–210, we performed (1) dose-recovery tests to evaluate the ability to recover a known laboratory dose and (2) preheat plateau tests to evaluate any dependence on temperature (Wintle and Murray, 2006). Both of the tests were conducted using three aliquots for each temperature step between 180° and 260 °C. The preheat test identified a plateau between 220° and 280 °C, and the protocol was able to recover a regenerated dose within 10% of unity at 260 °C (see supplementary material, Fig. S1). Based on these results, we chose to apply a preheat temperature of 260 °C and a cut-heat temperature of 220 °C.

#### 4.3. OSL data analysis

We used early background subtraction to calculate the  $D_e$  for all samples, i.e., the sum of the photons detected in the first 0.4 s or the first 0.23 s of the OSL decay curve for the Daybreak 2200 and Riso Readers, respectively, minus the sum of the next 1 s or 0.58 s, respectively. Given that some of the samples exhibited a medium component, use of early background subtraction isolates the fast component of the quartz.

Only aliquots (sub-samples) that satisfied the following criteria were used in the  $D_e$  calculation for small aliquot: (1) the OSL-IR depletion ratio was between 0.9 and 1.1, such that relative to OSL, no infrared signal exists above the background level (a response to infrared stimulation might signify contamination of the signal from feldspar) (Fig. 3C and F); (2) the recycling ratio was between 0.8 and 1.2 (Fig. S1C); (3) the recuperated OSL signal was less than 5% of the natural signal. Regenerative doses were fit with a saturating exponential equation to calculate the growth curve, or dose-response curve. The natural signal from each sample (fine-grain quartz) or aliquot (coarse-grain quartz) was then used to calculate the  $D_e$ .

#### 4.4. OSL dose-rate calculation

To calculate the dose rate for most samples, we used  $\sim 100$  g of sediment from the surrounding 30 cm of sediment. However, for one sample (Mayikake), the dose rate was only calculated using sediment in the tube. We quantified the concentrations of U, Th, K, and Rb using an ICP-MS, as well as the water content and cosmic ray contribution in each sample, with the exception of LED 11–356. For these samples, we measured the total alpha counts (Table 2) to calculate a bulk alpha rate from U and Th following the conversion factors in Aitken (1985) and determined the concentration of K. Elemental concentrations were measured at the ALS mineral lab in Reno, NV. Alpha counts were measured using 583 Daybreak alpha counters at the Institute of Geology, China Earthquake Administration, in Beijing, China. We note that both methods yielded relatively consistent results, with little variation in the dose rates across the region (see Table 2). An alpha efficiency of  $0.04 \pm 0.02$  for silt (4–11  $\mu\text{m}$ ) quartz (Rees-Jones, 1995) was used for the fine-grain dose-rate calculation. The cosmic-ray dose rate was calculated following Prescott and Hutton (1994).

The natural and saturated water content was measured in the laboratory. The possibility of time-varying water content was considered in more detail to calculate an average total dose-rate. We assumed the sediments were water-saturated when they were initially deposited. Because of the modern arid climate, the samples were nearly dry when we collected them, but we do not know at what point since initial deposition the samples were raised above the water table. Therefore, we consider a water content that varies from a completely dry sample (0% water content) to one with a saturated water content, by dividing the saturated water content in half and assigning a 100% error (Li et al., 2012, 2013). This range should cover all likely values.

#### 4.5. Choice of OSL age model

Several statistical procedures exist to determine the appropriate model to calculate the paleodose of incompletely bleached samples, e.g., Bailey and Arnold (2006), for single-grain and small-aliquot data. The central age model for normally distributed data (CAM: Galbraith et al., 1999) and minimum age model for skewed and scattered data (MAM: Galbraith et al., 1999) are the models most commonly applied to fluvial deposits. Other studies, e.g., Roberts et al. (2000) and Rodnight et al. (2006), have also employed the finite mixture model (FMM: Galbraith and Green, 1990) to determine a burial dose for heterogeneously bleached samples with discrete dose populations. For a recent review of statistical methods, see Galbraith and Roberts (2012) and Kunz et al. (2014).

The  $D_e$  distributions of all coarse-grain quartz samples are skewed, with a tail of higher  $D_e$  values, yet no negative  $D_e$  values. We follow the statistical procedures outlined in previous studies (Olley et al., 2004; Bailey and Arnold, 2006) to guide our choice of age model and determine an age for each terrace surface. Thus, to choose the appropriate age model, we relied on the degree of over-dispersion, absence of negative  $D_e$  values, skewness (Bailey and Arnold, 2006), and geomorphic context. OSL ages were calculated using the R Luminescence software package (Kreutzer et al., 2012) and Excel spreadsheets. OSL ages are presented with 1-standard-error.

### 5. Cosmogenic <sup>10</sup>Be depth profile sampling & analysis

Cosmogenic-nuclide depth profiling relies on the predictable decrease of the <sup>10</sup>Be concentration with depth below the surface. As long as initial aggradation was rapid compared to the age of the terrace and the surface has been stable since abandonment, a depth-dependent trend in the <sup>10</sup>Be concentration can be used to date the terrace surface and determine the inheritance (Anderson et al., 1996; Repka et al., 1997). We collected cosmogenic depth profiles from  $\sim 2$ -m-deep pits located on unmodified fluvial terrace surfaces (Anderson et al., 1996;

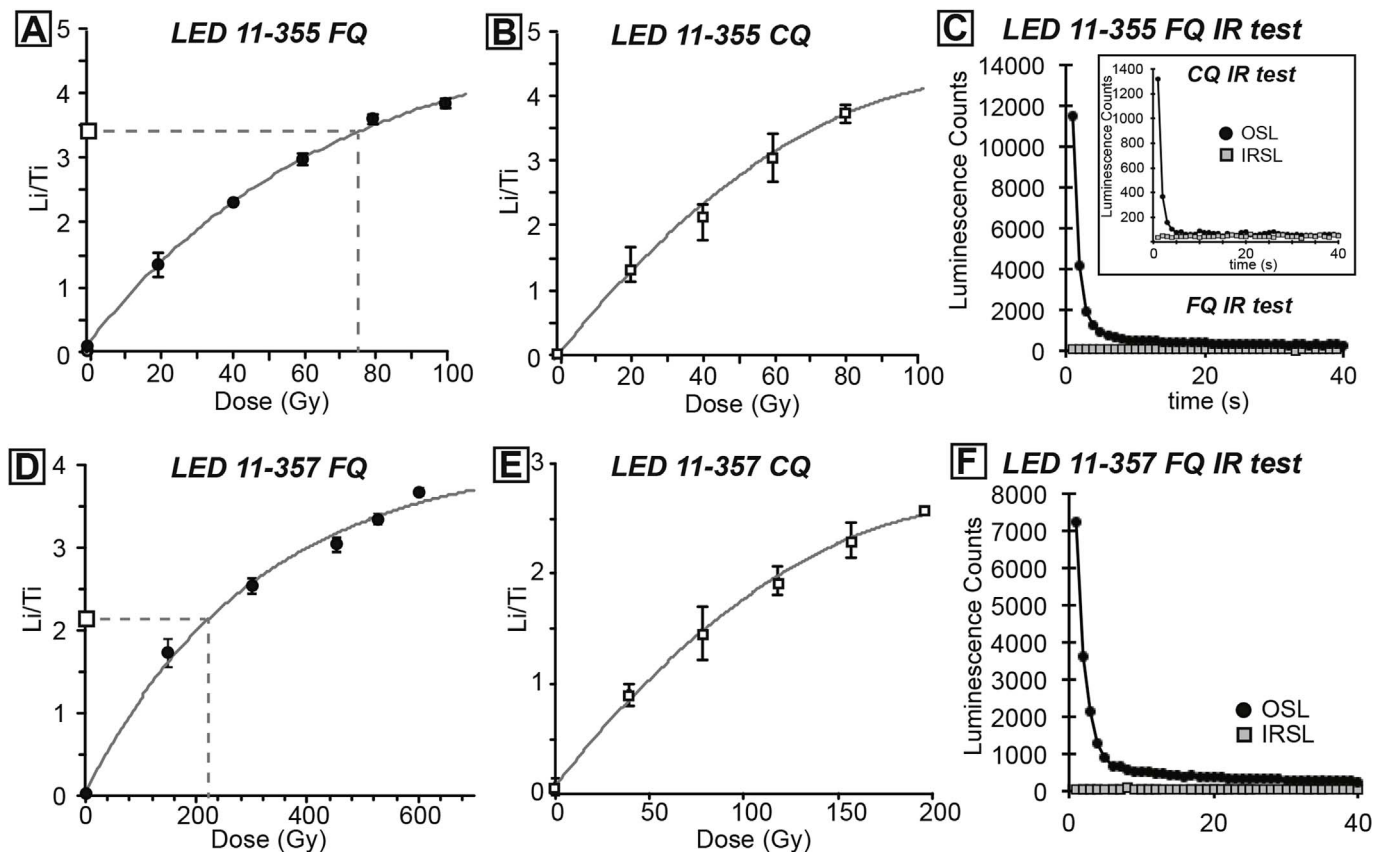


**Fig. 3.** (A) Dose-response curve for LED 11–355, following SMAR protocol (Lu et al., 2007) on 4–11 μm quartz. (B) Dose-response curve for LED 11–355, following SAR protocol (Murray and Wintle, 2000) on 90–180 μm quartz. (C) Natural OSL and IRSL shakedown curves for LED 11–355. Note low IRSL signals, indicating little to no feldspar contamination. Large plot is 4–11 μm quartz, inset shows 90–180 μm quartz. (D) Dose-response curve for LED 11–357, following SMAR protocol (Lu et al., 2007) on 4–11 μm quartz. (E) Dose-response curve for LED 11–357, following SAR protocol (Murray and Wintle, 2000) on 90–180 μm quartz. Note different scale than LED 11–357 fine-grain sample. (F) Natural OSL and IRSL shakedown curves for LED 11–357. Note low IRSL signals, indicating little to no feldspar contamination. Large plot is 4–11 μm quartz. Additional OSL and IRSL shakedown curves and dose-response curves shown in supplementary material.

**Table 2**  
Chemistry of OSL samples.

Sample No.	Bulk Alpha (ks-1.cm-2)	U (ppm)	Th (ppm)	K (%)	Rb (ppm)	SWC (%) <sup>a</sup>	WC (%) <sup>a</sup>	Dose rate (Gy/ka)	Dose rate <sup>d</sup> (Gy/ka)
<b>Mayikake</b>									
LED11-210	5.7 ± 0.1	1.4	4.8	0.94	38.6	31	15 ± 15	2.3 ± 0.6 <sup>b</sup>	1.5 ± 0.2
LED11-209	8.1 ± 0.2	2.0	6.8	1.45	62.5	29	14 ± 14	2.3 ± 0.6 <sup>b</sup>	–
LED11-355	4.9 ± 0.1	1.3	4.7	0.98	39.5	20	10 ± 10	2.1 ± 0.4 <sup>b</sup>	1.6 ± 0.1
LED11-356	5.8 ± 0.1	–	–	1.17	–	23	11 ± 11	2.3 ± 0.6 <sup>c</sup>	1.9 ± 1.3
<b>Mingyaole</b>									
LED11-360	6.0 ± 0.1	2.0	6.6	1.22	53.3	19	9 ± 9	2.3 ± 0.4 <sup>b</sup>	2.2 ± 0.2
LED11-357	4.8 ± 0.1	1.4	6.0	1.24	53.7	22	11 ± 11	2.1 ± 0.4 <sup>b</sup>	2.0 ± 0.2
LED11-359	5.3 ± 0.1	1.3	4.9	0.95	43.6	23	11 ± 11	1.7 ± 0.4 <sup>b</sup>	–
LED11-358	5.3 ± 0.1	1.5	3.7	0.77	32.6	24	12 ± 12	1.5 ± 0.2 <sup>b</sup>	–

<sup>a</sup> SWC stands for lab-measured saturated water content of the sample. WC stands for water content, defined as weight of water in sample/weight of dry sample. The water content assumes an average of 0% (dry sample) and measured saturated water content.

<sup>b</sup> Fine-grain dose-rate, calculated using U, Th, K, and Rb.

<sup>c</sup> Fine-grain dose-rate, calculated using bulk alpha counts (from U and Th) and K.

<sup>d</sup> Coarse-grain dose-rate, calculated using U, Th, K, and Rb, except for LED 11–356, which was calculated using the bulk alpha counts (from U and Th) and K.

Repka et al., 1997). The sand samples were collected at intervals of 30–40 cm at depths of 0, 30, 60, 90, 120, 160, and 200 cm below the top of the terrace surface by extracting the sand-sized fraction from the matrix of the gravel cover. Due to the lack of sand at the surface, we also collected a pebble sample from the surface, in addition to pebbles from 2-m depth to constrain the inheritance for the pebbles in comparison to that of sand of the same depositional age. Pebble clasts with diameters of 1–4 cm and high quartz content (primarily granite, vein quartz, and quartzite) were collected (~30 pebbles per depth) and

crushed. Both sand and pebble samples were sieved to ~0.25–1 mm.

We processed the samples at the Cosmogenic Radionuclide Target Preparation Lab at University of California, Santa Barbara, following standard laboratory procedures outlined in the UCSB Cosmogenic Radionuclide Target Preparation Facility Sample Preparation Manual (c.f. Bookhagen and Strecker, 2012). We verified the purity of the quartz using ICP-MS measurements of Al, which yielded concentrations of < 220 ppm in all samples. <sup>10</sup>Be measurements were made at Purdue Rare Isotope Measurement Laboratory (PRIME) Laboratory using the

07KNSTD standard (Nishiizumi et al., 2007).  $^{10}\text{Be}/^9\text{Be}$  ratios were corrected using a  $^{10}\text{Be}$  laboratory blank ( $n = 2$ ) of  $5.4 \times 10^{-15}$  atoms/g for depth-profile sand samples, and  $9.2 \times 10^{-15}$  atoms/g for pebble samples.

Using the Matlab Monte Carlo modeling program (v. 1.2) from Hidy et al. (2010) and CRONUS Earth 2.2 calculator (Balco et al., 2008), we calculated the age,  $^{10}\text{Be}$  inheritance, and surface erosion rate of each sand-and-pebble depth profile. We calculated cosmogenic  $^{10}\text{Be}$  ages following the constant (time-independent) scaling scheme of Lal (1991) and Stone (2000) and a reference spallogenic  $^{10}\text{Be}$  production rate of  $4.01 \pm 0.39$  atoms/g/a ( $1\sigma$ , Sea Level High Latitude – SLHL) (Borchers et al., 2015) scaled to our field site, a  $^{10}\text{Be}$  half-life of  $1.387 \times 10^6$  years (Korschinek et al., 2010), and an attenuation length of  $160 \text{ g/cm}^2$  (Gosse and Phillips, 2001). We measured topographic shielding in the field (Nishiizumi et al., 1989) and calculated shielding values using the CRONUS Earth 2.2 calculator (Balco et al., 2008). To account for a range of probable overall sediment densities, we applied a density of  $1.5\text{--}2.0 \text{ g/cm}^3$  in the Monte Carlo model based on field measurements. All  $^{10}\text{Be}$  depth profile ages and modeled parameters (i.e., inheritance, erosion rate, slip rates) are presented at the 95%-confidence level based on outputs from the Monte Carlo model.

In addition, field observations suggest that little erosion of the terrace surface has occurred since deposition. We did not observe any evidence of significant modification of the terrace surface, such as a fine-grain layer in the subsurface that might indicate inflation, a coarsening of material in the immediate subsurface that may indicate deflation, or the presence of cut-and-fill or other recent fluvial features that may represent erosion of the surface by small channels or overland flow. Therefore, we assigned the maximum surface-erosion depth to be  $\leq 10$  cm and limited the maximum erosion rate of the terrace surface to  $\leq 2$  cm/ka in the Monte Carlo model. This approach of placing limits on erosional parameters based on field evidence is a common practice (Hidy et al., 2010; Haghypour et al., 2012). Below we discuss the uncertainties associated with varying these parameters (section 7.3).

## 6. Results

In total, 5 coarse-grain and 8 fine-grain quartz OSL samples were measured (Tables 1–3, Figs. 2, Fig. 3, Fig. 4). Coarse-grain and fine-grain samples were taken from the same sampling tube and have the

same respective sample numbers. All samples had enough fine-grain material for analysis; however, only 5 samples had enough coarse-grain quartz for analysis. Sixty aliquots were measured for each coarse-grain quartz sample, with the exception of LED 11–356, from which we measured 94 aliquots. Accepted aliquots ranged from 18 for LED 11–210 to 46 for LED 11–360 (Table 3). The  $D_e$  distributions of the coarse-grain samples (Fig. 4) are skewed, with tails of high  $D_e$  values. Furthermore, well-bleached samples typically have an overdispersion of  $\sim 20\%$  (Arnold and Roberts, 2009), whereas all of the coarse-grain quartz samples that we analyzed had overdispersion values ranging from 28 to 58% (Table 3), which may also arise from the use of multiple-grain aliquots and mask the true signal distribution. Based on our  $D_e$  distributions and the observed overdispersion, heterogeneous bleaching appears to be an issue for all of the samples. Thus, the minimum age model (MAM) became our age model of choice (Galbraith et al., 1999), using a  $\sigma_b$  value of 0.1. In section 7.2, we discuss the effect different  $\sigma_b$  values have on the MAM age calculations. We also applied the central age model (CAM) (Table 3) to compare to the fine-grain samples, which were calculated using only the CAM given the low number ( $n = 10\text{--}12$ ) of aliquots measured in the SMAR protocol (Lu et al., 2007). This protocol does not allow for a full evaluation of the  $D_e$  distribution, because the multiple aliquot approach averages inter-aliquot variations that may have persisted despite the use of multiple-grain aliquots. To calculate ages for each terrace, we take the error-weighted average of all coarse-grain quartz OSL samples following the MAM.

The cosmogenic nuclide depth profiles yielded ages for both sand- and pebble-depth profiles on both the Mayikake and Mingyaole terraces.

### 6.1. Mayikake

At Mayikake, we dated 4 fine-grain and 3 coarse-grain OSL samples, in addition to the cosmogenic  $^{10}\text{Be}$  depth profile that consisted of 6 sand samples and 2 pebble samples. The Mayikake fine-grain samples ( $n = 4$ ) yield a mean CAM age of  $23.2 \pm 1.4$  ka (Table 3). The 3 coarse-grain quartz samples yielded a CAM age of  $25.5 \pm 1.8$  ka and a MAM age of  $16.2 \pm 0.8$  ka (Table 3).

The cosmogenic  $^{10}\text{Be}$  depth profile based on detrital sand yielded an age of  $14.2^{+3.0}_{-4.4}$  ka (Table 4, Table 5, Fig. 5A). The best-fit, model-derived surface erosion rate for the terrace is 6 mm/ka. The pebble

**Table 3**  
OSL dating results.

Sample No.	Aliquots <sup>a</sup>	$D_0$ (Gy)	Over-dispersion <sup>b</sup>	CAM <sup>c</sup> $D_e$ (Gy)	CAM age (ka)	MAM <sup>d</sup> $D_e$ (Gy)	MAM age (ka)
<b>Mayikake</b>							
LED11-210FQ <sup>e</sup>	10	80	–	$61.5 \pm 2.6$	$21.3 \pm 2.2$	–	–
LED11-209FQ	10	97	–	$61.9 \pm 3.4$	$21.4 \pm 2.5$	–	–
LED11-355FQ	11	67	–	$76.5 \pm 13.8$	$36.4 \pm 7.2$	–	–
LED11-356FQ	11	182	–	$68.3 \pm 7.2$	$29.7 \pm 3.9$	–	–
LED11-210SA <sup>f</sup>	18 (60)	112	$28.0 \pm 4.9$	$42.3 \pm 2.1$	$27.4 \pm 3.5$	$32.1 \pm 2.8$	$20.9 \pm 2.0$
LED11-355SA	19 (60)	152	$40.2 \pm 6.5$	$38.1 \pm 3.5$	$23.7 \pm 3.1$	$21.0 \pm 2.5$	$13.0 \pm 1.6$
LED11-356SA	35 (94)	183	$31.8 \pm 4.0$	$45.4 \pm 2.5$	$25.8 \pm 2.9$	$29.0 \pm 0.5$	$16.5 \pm 1.7$
<b>Mingyaole</b>							
LED11-360FQ	12	217	–	$259.9 \pm 36.4$	$113.0 \pm 18.0$	–	–
LED11-357FQ	12	310	–	$229.5 \pm 22.5$	$111.0 \pm 15.4$	–	–
LED11-359FQ	11	326	–	$215.0 \pm 20.8$	$126.5 \pm 16.9$	–	–
LED11-358FQ	12	240	–	$309.2 \pm 17.9$	$208.5 \pm 31.8$	–	–
LED11-357SA	36 (60)	–	$58.1 \pm 7.0$	$56.3 \pm 6.4$	$28.5 \pm 4.3$	$26.0 \pm 2.7$	$13.2 \pm 1.4$
LED11-360SA	45 (60)	86	$52.0 \pm 5.8$	$44.7 \pm 3.6$	$20.5 \pm 2.4$	$18.6 \pm 1.7$	$8.5 \pm 0.9$

<sup>a</sup> Number of accepted aliquots used in equivalent dose ( $D_e$ ) calculations, out of total aliquots measured.

<sup>b</sup> All errors in table are 1 standard error.

<sup>c</sup> CAM – central age model.

<sup>d</sup> MAM – minimum age model. Results show here are MAM-3 model. MAM-4 results are similar but not shown, as p-value was near 0, indicating the MAM-4 model is not a good match for the distribution.

<sup>e</sup> FQ – fine-grain quartz.

<sup>f</sup> SA – small-aliquot coarse-grain quartz.

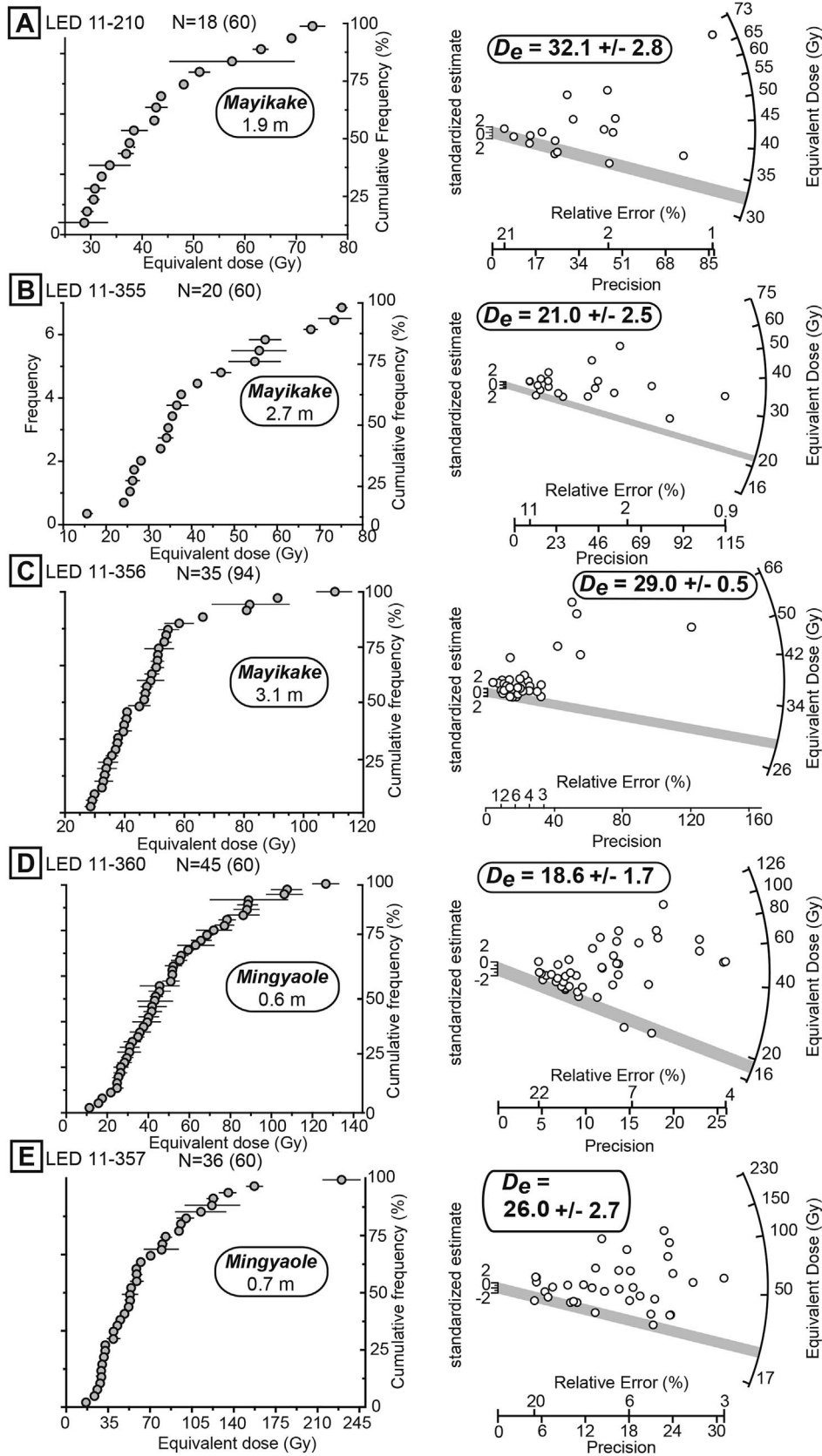


Fig. 4. Coarse-grain quartz OSL sample data. (A–E) Left-hand panels are cumulative frequency (grey circles, with 1 standard error). N is the number of accepted aliquots (out of total aliquots measured). Right-hand panels are radial plots of the same data.  $D_e$  are listed with 1 standard error.



**Table 4**  
Cosmogenic beryllium-10 data.

Sample No.	Latitude/Longitude	Elevation (m)	Depth (m)	Thickness (cm) <sup>a</sup>	Mass qtz (g)	<sup>10</sup> Be/ <sup>9</sup> Be (10 <sup>-14</sup> ) <sup>bc</sup>	<sup>9</sup> Be carrier (mg) <sup>b</sup>	[ <sup>10</sup> Be] (10 <sup>4</sup> atoms g <sup>-1</sup> )
<b>Mayikake Depth Profile (detrital sand)</b>								
MYK-6	39.5836°N/75.1046°E	1869	0.3	5	30.18	31.6 ± 0.88	0.252	17.7 ± 1.51
MYK-5	39.5836°N/75.1046°E	1869	0.6	5	40.98	30.6 ± 0.83	0.252	12.6 ± 1.07
MYK-4	39.5836°N/75.1046°E	1869	0.9	5	43.64	23.5 ± 0.59	0.249	8.96 ± 0.76
MYK-3	39.5836°N/75.1046°E	1869	1.2	5	30.69	12.3 ± 0.36	0.250	6.68 ± 0.57
MYK-2	39.5836°N/75.1046°E	1869	1.6	5	43.88	12.5 ± 0.44	0.245	4.66 ± 0.41
MYK-1	39.5836°N/75.1046°E	1869	2.0	5	60.76	12.2 ± 0.43	0.251	3.37 ± 0.29
<i>Pebble Samples (1–3 cm)</i>								
MYK-7p	39.5836°N/75.1046°E	1869	0	1.5	95.38	131.0 ± 8.39	0.261	24.0 ± 2.48
MYK-1p	39.5836°N/75.1046°E	1869	2.0	5	56.09	12.3 ± 0.79	0.267	3.32 ± 0.34
<b>Mingyaole Depth Profile (detrital sand)</b>								
MYL-6	39.4838°N/75.3821°E	1670	0.3	5	53.53	46.9 ± 0.84	0.225	13.2 ± 1.09
MYL-5	39.4838°N/75.3821°E	1670	0.6	5	47.24	32.7 ± 0.62	0.256	11.8 ± 0.98
MYL-4	39.4838°N/75.3821°E	1670	0.9	5	34.73	18.2 ± 0.60	0.257	9.0 ± 0.78
MYL-3	39.4838°N/75.3821°E	1670	1.2	5	48.95	23.9 ± 0.67	0.263	8.6 ± 0.74
MYL-2	39.4838°N/75.3821°E	1670	1.6	5	54.34	22.0 ± 0.70	0.253	6.85 ± 0.59
MYL-1	39.4838°N/75.3821°E	1670	2.0	5	46.92	16.8 ± 0.65	0.263	6.3 ± 0.56
<i>Pebble Samples (1–3 cm)</i>								
MYL-7p	39.4838°N/75.3821°E	1670	0	1.5	50.08	89.0 ± 3.65	0.255	17.4 ± 1.58
MYL-1p	39.4838°N/75.3821°E	1670	2.0	5	57.72	21.3 ± 1.17	0.236	4.98 ± 0.49

<sup>a</sup> Thickness is the height of the unit (in cm) from which the sample was collected, for sand and pebble samples from depth profiles. Thickness for surface pebble samples refers to the average diameter of a pebble at the surface.

<sup>b</sup> Isotope ratios were normalized to <sup>10</sup>Be standards prepared by Nishiizumi et al. (2007) with a value of 2.85 × 10<sup>12</sup> and a <sup>10</sup>Be half-life of 1.387 × 10<sup>6</sup> years (Korschinek et al., 2010).

<sup>c</sup> <sup>10</sup>Be/<sup>9</sup>Be ratios were corrected using a <sup>10</sup>Be laboratory blank (n = 2) of 5.4 × 10<sup>-15</sup> atoms/g for depth profile sand samples, and 9.2 × 10<sup>-15</sup> atoms/g for pebble samples.

samples yielded an equivalent age of 14.2<sup>+2.8</sup>/<sub>-4.0</sub> ka (Fig. 5A). The inheritances for the sand and pebble fractions were 0.68<sup>+1.47</sup>/<sub>-0.68</sub> × 10<sup>4</sup> atoms/g and 0.68<sup>+1.17</sup>/<sub>-0.68</sub> × 10<sup>4</sup> atoms/g, respectively (Table 5).

Within error, the CRN ages and coarse-grain MAM ages agree. These ages suggest the terrace cover was deposited until ~12–14 ka and then abandoned abruptly after deposition (Fig. 6A).

Using the CRN abandonment age for the Mayikake surface, a scarp height and fault dip of 38 m and 75° ± 5° for the Bieertuokuoyi Frontal Thrust (PFT) (Fig. 7A and B) and a scarp height and fault dip of 15 m and 16° ± 3° for the Mayikake Thrust (Fig. 7C and D) that deform this surface, we calculate dip-slip rates of 2.6<sup>+2.1</sup>/<sub>-0.5</sub> mm/a and 3.7<sup>+2.8</sup>/<sub>-1.4</sub> mm/a, respectively, for these faults. Given observations on regional seismic lines, we assume the faults merge into a subhorizontal decollement at depth (Chen et al., 2010; Li et al., 2012; Wang et al., 2016). Given the strike-slip component on the Bieertuokuoyi Frontal Thrust described by Li et al. (2012), its estimated total shortening rate is ~4.6 mm/a, whereas for the Mayikake Thrust, the estimated shortening rate is ~3.7 mm/a.

### 6.2. Mingyaole

From the Mingyaole terrace, we collected 4 OSL samples, of which we dated all four using the fine-grain component, but only dated two with the coarse-grain component. In addition, we collected a cosmogenic <sup>10</sup>Be depth profile that consisted of 6 sand samples and 2 pebble samples. Three fine-grain samples from the Mingyaole surface yield an average CAM age of 117.8 ± 8.0 ka, with a fourth sample yielding an age of 208.5 ± 24.2 ka (Table 3). Notably, all ages were in stratigraphic order. We interpret that the oldest sample may be near saturation or incompletely bleached, because that sample is nearly 100 ka older than the remaining three samples, yet it lies only 0.2–0.4 m stratigraphically deeper. Moreover, no intervening erosion surfaces or soils were observed in the field or in the cosmogenic depth profile (Fig. 6B). Notably, fine-grain quartz may begin to saturate around 200–300 Gy (Timar-Gabor and Wintle, 2013). Sample LED 11–358 has a D<sub>e</sub> of 309.2 Gy, yet a D<sub>0</sub> of 240 Gy (Table 3), suggesting it is likely saturated. Alternatively, this older age may also be a result of a different dose-rate history (Table 3), or sediment that experienced a

**Table 5**  
Cosmogenic beryllium-10 data and ages.

Sample No.	Production Rate (atoms/g/a)		Shielding Correction <sup>c</sup>	Erosion rate (cm/a) <sup>d</sup>	Inheritance (10 <sup>4</sup> atoms/g)	Age (ka) (95% CI) <sup>e</sup>
	Spallation <sup>a</sup>	Muons <sup>b</sup>				
<b>Ages based on sand samples from 0.3–2 m depth</b>						
Mayikake	16.26	0.330	0.98	0.0006	0.68 <sup>+1.47</sup> / <sub>-0.68</sub>	14.2 <sup>+3.0</sup> / <sub>-4.4</sub>
Mingyaole	14.10	0.311	0.98	0.0014	5.09 <sup>+1.82</sup> / <sub>-2.37</sub>	8.5 <sup>+4.3</sup> / <sub>-5.0</sub>
<b>Ages for pebbles from 2 m depth and the surface</b>						
Mayikake	16.26	0.330	0.99	0.0006	0.68 <sup>+1.17</sup> / <sub>-0.68</sub>	14.2 <sup>+2.8</sup> / <sub>-4.0</sub>
Mingyaole	14.10	0.311	0.98	0.0014	3.21 <sup>+1.28</sup> / <sub>-1.51</sub>	10.4 <sup>+2.6</sup> / <sub>-3.5</sub>
<b>Ages based on sand and pebble samples</b>						
Mayikake	16.26	0.330	0.98	0.0005	0.57 <sup>+1.58</sup> / <sub>-0.57</sub>	14.2 <sup>+3.0</sup> / <sub>-4.4</sub>
Mingyaole	14.10	0.311	0.98	0.0012	4.34 <sup>+1.72</sup> / <sub>-2.26</sub>	9.4 <sup>+4.2</sup> / <sub>-4.5</sub>

<sup>a</sup> Constant (time-invariant) local production rate based on Lal (1991) and Stone (2000). A sea level, high latitude production rate of 4.01 <sup>10</sup>Be atoms/g/a quartz was used (Borchers et al., 2015).

<sup>b</sup> Constant (time-invariant) local production rate based on Heisinger et al. (2002a, b).

<sup>c</sup> Geometric shielding correction for topography calculated with the Cosmic-Ray Produced Nuclide Systematics (CRONUS) Earth online calculator (Balco et al., 2008) version 2.2 (<http://hess.ess.washington.edu/>).

<sup>d</sup> Erosion rate and inheritance from best fit Monte Carlo model of Hidy et al. (2010).

<sup>e</sup> Bayesian most probable age from Monte Carlo model of Hidy et al. (2010), with 95% upper and lower bounds.

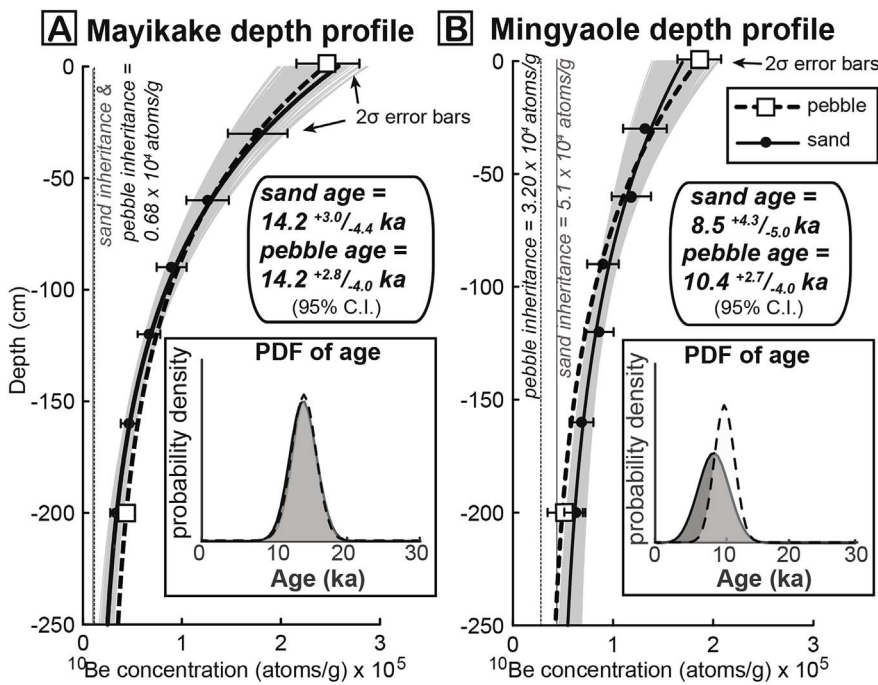


Fig. 5. Cosmogenic  $^{10}\text{Be}$  depth profile for A) Mayikake terrace surface and B) Mingyaole terrace surface. Circles represent  $^{10}\text{Be}$  concentration of sand samples, with  $1\sigma$  uncertainties. Squares represent  $^{10}\text{Be}$  concentrations of pebble samples, with  $1\sigma$  uncertainties. Solid and dashed black lines are the lines of best fit through the sand and pebble sample data, respectively, with grey lines representing the 95% confidence interval of the line of best fit for the sand samples for Mayikake and Mingyaole calculated using the Monte Carlo model of Hidy et al. (2010). Insets show probability density functions of the age from the Monte Carlo model. Solid black line with dark grey fill represents sand age distribution, dashed black line with light grey fill represents pebble age distribution. Modeled inheritance values for each site shown as dashed vertical lines.

different transport process, such that fewer grains were bleached during transport in the fluvial system, e.g., eroded from a nearby source at night, as discussed in further detail in the discussion. Regardless, we chose to use the three youngest ages to characterize the fine-grain age ( $\sim 118$  ka) of the Mingyaole surface (Fig. 6B). On the same Mingyaole terrace, the average coarse-grain quartz CAM and MAM OSL ages are  $22.4 \pm 2.1$  and  $9.9 \pm 0.8$  ka (Fig. 6B, Table 3), respectively.

The cosmogenic  $^{10}\text{Be}$  depth profile based on detrital sand yielded an age of  $8.5^{+4.3}_{-5.0}$  ka (Table 4, Table 5, Fig. 5B). The best-fit, modeled-derived surface erosion rate is 14 mm/ka. The pebbles samples at the surface yielded a similar age of  $10.4^{+2.6}_{-3.5}$  ka (Fig. 5B). The inheritances for the sand and pebble fractions were  $5.09^{+1.82}_{-2.37} \times 10^4$  atoms/g and  $3.21^{+1.28}_{-0.51} \times 10^4$  atoms/g, respectively (Table 5).

The CRN ages and coarse-grain MAM ages agree well. These ages suggest the terrace cover was deposited until  $\sim 8\text{--}10$  ka and then abandoned shortly thereafter: approximately 8.5 ka (Fig. 6B).

Using the CRN sand depth-profile age of  $\sim 8.5$  ka and an incremental shortening of  $\sim 10.1$  m, we calculate a shortening rate of  $1.2^{+3.9}_{-0.3}$  mm/a for the southern limb of the Mingyaole anticline following the equations outlined in Li et al. (2015b) (Fig. 7E and F). If we assume the northern limb is shortening at the same rate (Scharer et al., 2006), we calculate an overall shortening rate of  $\sim 2.4$  mm/a for the Mingyaole anticline since the terrace abandonment age of  $\sim 8.5$  ka.

## 7. Discussion

### 7.1. OSL grain size-dependent age differences

In the western Tarim Basin, we observe that fine-grain OSL samples likely overestimate the depositional age of a terrace (Fig. 6). On Mayikake, the fine-grain CAM ages agree with the coarse-grain CAM ages within error. In contrast, the fine-grain CAM ages from the

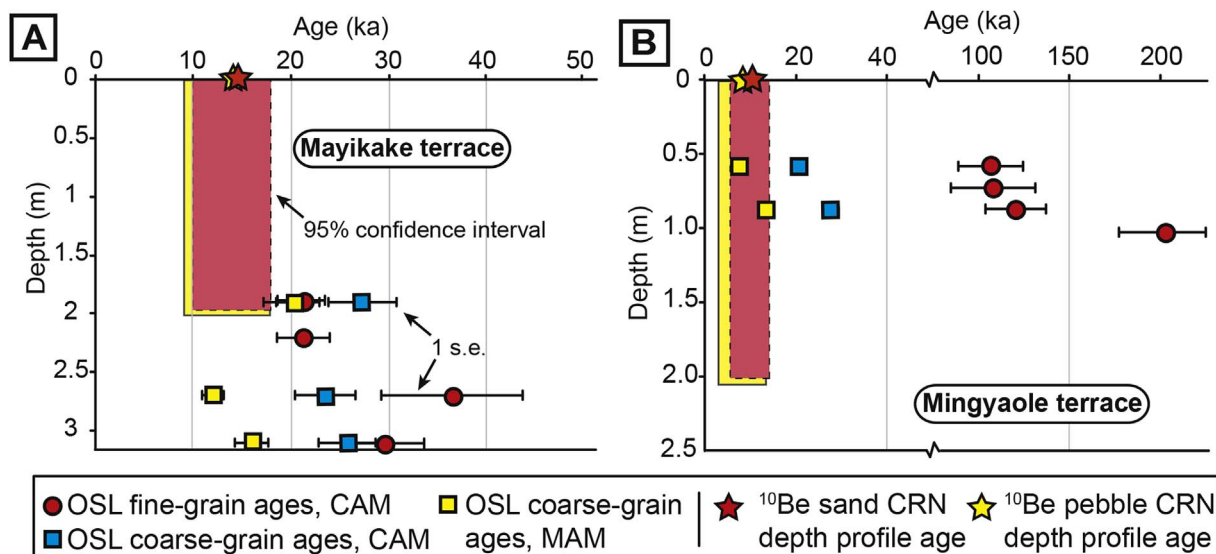


Fig. 6. Age-depth profiles for each site, comparing OSL ages calculated using the two different age models (discussed in text) and cosmogenic  $^{10}\text{Be}$  sand and pebble depth-profile ages. (A) Mayikake terrace. (B) Mingyaole terrace. CAM – central age model, MAM – minimum age model. OSL error bars are 1 standard error,  $^{10}\text{Be}$  error bars are 95% confidence intervals.

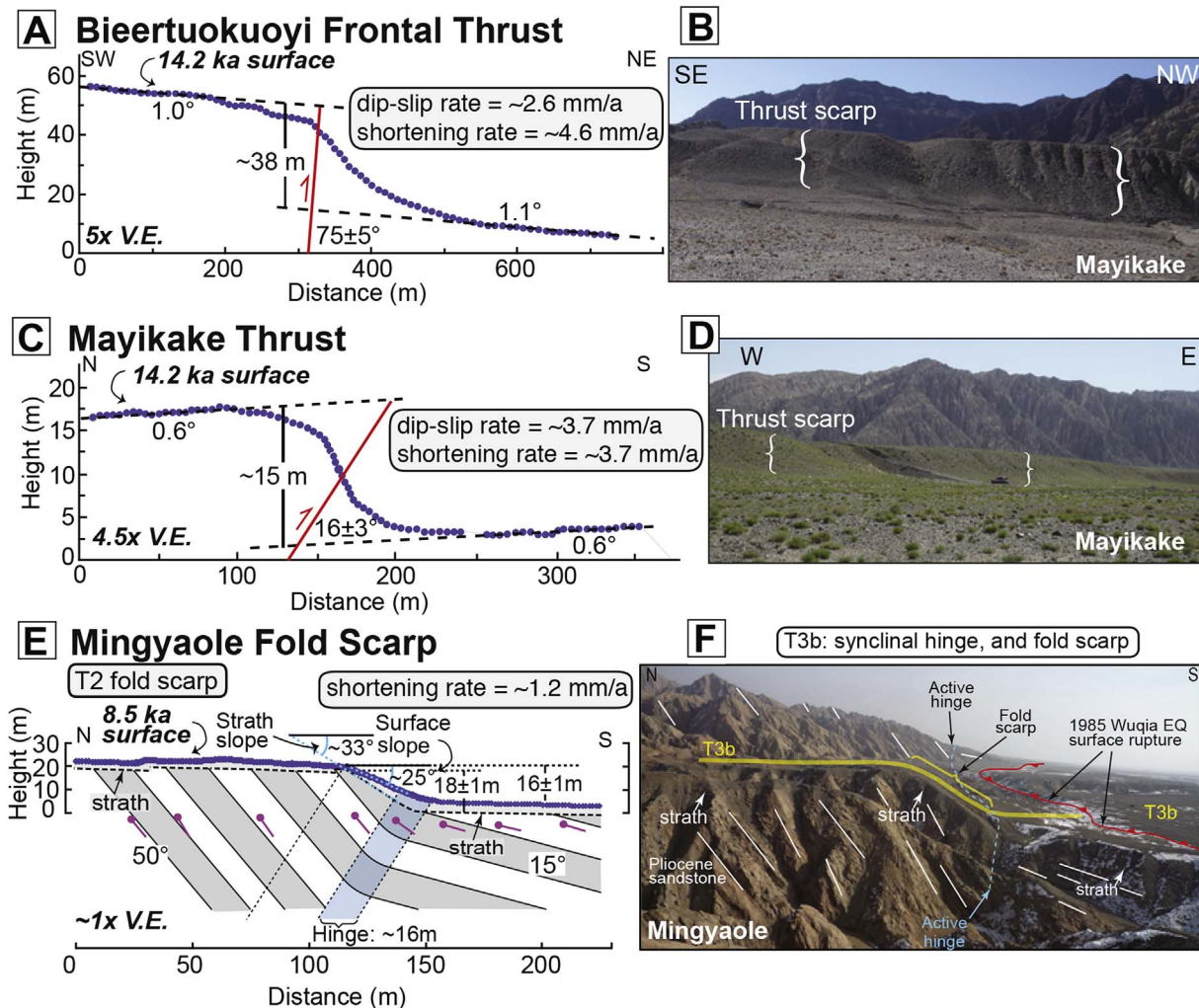


Fig. 7. (A) dGPS topographic profile and (B) field photo of the Biertuokuoyi Frontal Thrust on the Mayikake surface. Modified from Li et al. (2012). (C) dGPS topographic profile and (D) field photo of the Mayikake Thrust on the Mayikake surface. Modified from Li et al. (2012). (E) dGPS topographic profile of the T2 surface and (F) field photo of the T3b surface of the Mingyaole fold scarp. Modified from Li et al. (2015b). See Fig. 2 for locations of dGPS profiles and field photos.

Mingyaole surface overestimate the coarse-grain CAM age by  $\sim 100$  ka (a factor of ten). This discrepancy may arise for several reasons: (1) different aliquot sizes, leading to a different number of grains per disc (Wallinga, 2002; Duller, 2008); (2) insufficient bleaching of the finer grains, leading to the retention of residual doses that result in an overestimation of ages; (3) differences in the sources of the silt and sand grain-size fractions, leading to intrinsic differences in the way the quartz behaves. Below, we discuss the bleaching of grains in the western Tarim Basin. We do not have the required data to discuss different sources of the fine-vs. coarse-grains, but we suggest this potential contrast as an avenue for future research in this region.

#### 7.1.1. Aliquot size

Apart from the applied SMAR protocol, the apparent overestimation of the fine-grain OSL ages may result from the different aliquot sizes used for fine- and coarse-grain dating (diameters of 9.7 mm for fine-grain, and 2 mm for coarse-grain). The differences in both aliquot size and grain size result in large differences both in the number of grains on each disc and in the grains that contribute to the luminescence signal. Almost one million grains are present on each fine-grain aliquot: an abundance that averages out any grain-to-grain dose variations (Wallinga, 2002; Duller, 2008), but that can also result in an overestimation of the true depositional age of the sediment. Furthermore, the aliquot size effect is worsened by the use of the SMAR protocol,

which not only averages more grains per aliquot, but also averages interaliquot variation. The small-aliquot, coarse-grain quartz samples (90–180  $\mu\text{m}$ ) have  $\sim 200$ –300 grains per disc, and only 1.5–3.6% of the grains from nearby sites emit a luminescence signal (Yang et al., 2017). In homogeneously bleached depositional settings, averaging the dose variations has little effect on the age, but an apparent dose overestimation typifies heterogeneously bleached depositional settings (Arnold and Roberts, 2009; Cunningham et al., 2011).

#### 7.1.2. Bleaching of different grain sizes

In semi-arid to arid settings, most of the terrestrial sediment transport and deposition occurs during storms, which can have short, high-flow durations of a few hours, e.g., Porat et al. (2001) and Cohen and Laronne (2005). Sediment-laden flash-flood waters are turbid and may not occur during daylight hours, which may limit penetration of any sunlight and inhibit bleaching of the grains (Berger and Luternauer, 1987; Sanderson et al., 2007; Gray and Mahan, 2014). As a result, fine grains traveling as suspended load may not be exposed to sunlight long enough to be fully bleached prior to deposition (Sanderson et al., 2007). In such cases, most bleaching likely occurs during transient storage in bars along the river, instead of during transport (Gray and Mahan, 2014). Furthermore, fine-grains tend to flocculate and form aggregates, possibly due to mud coatings, which further hinders solar bleaching even when episodic flows occur during daylight (Rittenour, 2008; Hu et al., 2010; Gray and Mahan, 2014). In the western Tarim Basin, fine-

grain sediment in the rivers is commonly transported during episodic, short-lived floods that may erode proximal older geomorphic surfaces and weakly consolidated, exhumed Tertiary bedrock.

Coarser sediment, such as fine sand, is more likely to have been transported as saltating bedload and to spend a longer time exposed on channel bars between floods, especially if traveling as a continuous flow in waters with lower sediment concentration (Gray and Mahan, 2014). We observe that active bars in the Tarim channels are primarily sands. Recent work by Cunningham et al. (2015) tentatively suggests that coarse grains on bars or near the channel edge are likely to be better bleached because of the opportunities for reworking near the surface. Thus, coarse grains deposited repeatedly on exposed bars are likely to get reworked by both wind and water and to be thoroughly bleached as they travel through the fluvial system.

We speculate that river characteristics, especially in arid settings, likely have a dominant effect on the bleaching of fluvial sediments. In our study, OSL data from the Mayikake terrace – a terrace likely deposited by the Bieertuokuoyi River – indicate the sediments are more thoroughly bleached, with overdispersion varying between 28 and 40% and fine-grain and coarse-grain CAM ages in general agreement. The Bieertuokuoyi River is generally shallow and has clear water when not in flood. In contrast, the Kezilesu River (meaning “Red River”), which deposited the Mingyaole terrace, has a typical red-brown color due to its high suspended-sediment load and deeper water depths. The OSL data from the Mingyaole terrace display both higher overdispersion values of 50–58% and a larger discrepancy between the fine- and coarse-grain CAM ages. We conclude that the grains are heterogeneously bleached. Although the current river characteristics may not be indicative of the river characteristics over the last 100 ka, the OSL data indicate that, in general, deposits from the Bieertuokuoyi River are better bleached (sediments in the Mayikake Basin, this study; Li et al., 2012) than deposits from the Kezilesu River, e.g., sediments near the Mingyaole anticline (this study; Li et al., 2015b) and Mushi anticline (Li et al., 2013).

These observations and data, although based on a small sample set, suggest that rivers with higher suspended sediment load and deeper water depths are less likely to fully bleach sediments during transport (Berger, 1990; Berger and Leternauer, 1987; Gray and Mahan, 2014), especially the fine-grain fraction that is more likely to be traveling as suspended sediment during sediment-laden flash floods in semi-arid to arid settings.

## 7.2. OSL MAM age uncertainties arising from choice of $\sigma_b$

The  $\sigma_b$  parameter of the MAM is defined as the overdispersion of a well-bleached natural sample from a given field area. In the absence of direct data, Galbraith and Roberts (2012) recommend using overdispersion values of 10–20%, values that are approximately equal to many of the  $\sigma_b$  values for individual aliquots and quartz grains in the literature (Arnold and Roberts, 2009). Given that we do not have a well-bleached sample from our field area from which to calculate  $\sigma_b$ , we chose 0.1 because this value represents the overdispersion of the first regenerated dose for all the accepted aliquots. This value should be representative of the intrinsic overdispersion of the quartz that we are able to detect from our samples. Moreover, we also note that our choice of  $\sigma_b$  is similar to other studies on alluvial and fluvial sediments in arid/semi-arid settings, which use a value of  $\sim 0.1$  (0.1–0.15) (Fattahi et al., 2010; Colarossi et al., 2015).

However, given that we cannot directly calculate  $\sigma_b$ , we tested the sensitivity of our ages to our choice of  $\sigma_b$  by re-running the MAM calculations using  $\sigma_b$  values of 0.1, 0.2, 0.3, and 0.4 (Table S3, Table S4), which are common values for fluvial sediments in the literature (Fattahi et al., 2010; Trauerstein et al., 2014; Colarossi et al., 2015; Wang et al., 2015). Using a  $\sigma_b$  of 0.4 yields MAM  $D_e$ 's that are  $\sim 10$ – $20$  Gy higher (Table S3) and MAM ages that are  $\sim 5$ – $10$  ka older (Table S4) than using a  $\sigma_b$  of 0.1, with the exception of LED 11-356, which has an age

that is  $\sim 20$  ka older. Using a  $\sigma_b$  of 0.2 results in MAM  $D_e$ 's that are, on average,  $\sim 2$ – $4$  Gy higher (Table S3) and MAM ages that are  $\sim 1$ – $3$  ka older than using a  $\sigma_b$  of 0.1. A larger  $\sigma_b$  value of up to 0.4 increases the mean age of the Mayikake and Mingyaole surfaces up to  $24.9 \pm 2.2$  and  $15.2 \pm 2.1$  ka, respectively. Importantly, changing the MAM ages and mean ages for the surfaces by  $\sim 1$ – $10$  ka does not significantly change the tectonic and climatic implications of this study: the derived slip rates rely on the better-constrained CRN abandonment ages on Mingyaole and Mayikake, and the ages still broadly correlate with climatic events, within error (see section 8.2). However, if a larger  $\sigma_b$  value of 0.4 were used, the coarse-grain OSL MAM and CAM ages from Mayikake would agree, but the fine-grain OSL CAM ages on Mayikake and all OSL CAM ages on Mingyaole are still older (with the exception of LED11-210). Based on our above reasoning, we suggest that a  $\sigma_b$  of 0.1 or 0.2 is acceptable for our dataset.

## 7.3. Cosmogenic $^{10}\text{Be}$ age uncertainties

The age we calculate from the Monte Carlo model (Hidy et al., 2010) is sensitive both to the surface erosion rate since deposition and to the limits placed on the total, post-depositional erosion magnitude. Importantly, if the erosion rate and erosion magnitude are allowed to vary in an unconstrained manner, the Monte Carlo model yields a best-fit erosion rate of 2–3 cm/ka, a total erosion of  $\sim 20$ – $40$  cm, and an age that is 1–3 ka older than if the model uses a more constrained erosion rate and magnitude (as described in Section 5). Notably, these ages with unconstrained errors are still within the 95%-confidence intervals of the ages calculated with constrained parameters. Because field observations indicate no significant erosion, deflation, or inflation of the surface, we use ages calculated with a maximum erosion rate of 2 cm/ka, and a maximum total erosion of 10 cm. The best-fit erosion rate from the Monte Carlo Model was 0.6 cm/ka for Mayikake and 1.4 cm/ka for Mingyaole. However, we acknowledge that a wetter climate during the late Pleistocene and early-mid Holocene (Yang and Scuderi, 2010) might have created conditions with higher erosion rates for a period of time soon after the terraces were deposited and abandoned. Importantly, exponential trends of the concentrations with depth are consistent with continuous and rapid initial aggradation.

## 8. Regional implications

### 8.1. Deformation rates

The deformation rates calculated on the three structures reveal rapid, shortening during the late Quaternary across the NE Pamir margin (Li et al., 2012) (Fig. 7). Furthermore, the shortening rate across the NE Pamir margin since 0.35 Ma appears to be steady (Li et al., 2012), even though the deformation appears to be accommodated on different structures through time. Over timescales of  $\sim 98$  ka, the shortening rate averages  $> \sim 5.6$  mm/a on the Pamir Frontal Thrust (Thompson Jobe et al., 2017). On a shorter timescale (since the Last Glacial Maximum), the shortening rate ( $\sim 8$  mm/a) is similar across the same region of the northern margin of the Pamir, but is accommodated on two structures: the Bieertuokuoyi Frontal Thrust ( $\sim 4.6$  mm/a) and the Mayikake Thrust ( $\sim 3.7$  mm/a). These rates are similar to the rate since 0.35 Ma of  $\sim 6.4$  mm/a (Li et al., 2012), and the modern geodetic shortening rate of 6–9 mm/a (Zubovich et al., 2010; Li et al., 2012). Thus, these new results support the idea that the NE Pamir margin has experienced a relatively uniform shortening rate of 6–9 mm/a since 0.35 Ma (Li et al., 2012; Thompson Jobe et al., 2017). The deformation may be accommodated on different structures through time, as shortening shifts spatially from the Pamir Frontal Thrust  $\sim 98$  ka to being partitioned on both the Bieertuokuoyi Frontal Thrust and the Mayikake Thrust since  $\sim 15$  ka (Thompson Jobe et al., 2017).

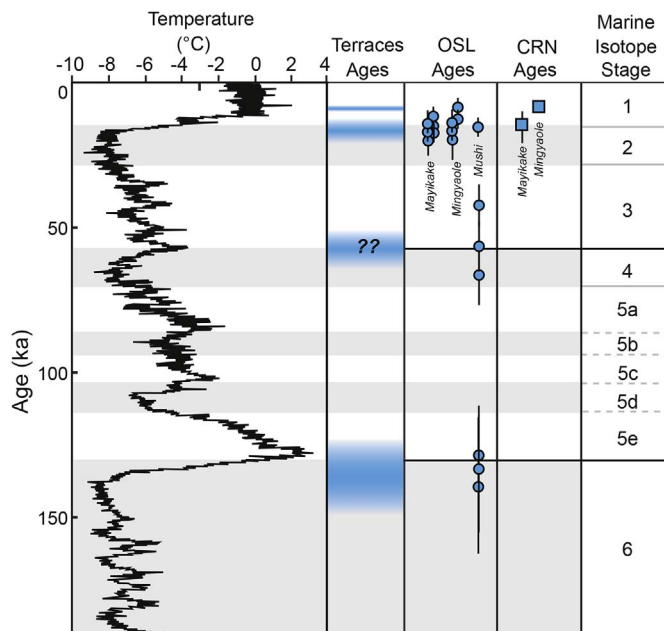


Fig. 8. Regional terrace correlations. Published terrace OSL ages and ages from this study shown with Vostok ice-core record from Petit et al. (1999). Glacial periods highlighted with light grey box. OSL ages shown as blue circles with 1 standard error uncertainty. CRN ages are shown as blue squares with 95% confidence interval. Approximate timing of terrace deposition and abandonment, based on OSL and CRN ages, shown as blue bars, and commonly align with glacial-interglacial transitions. OSL ages for Mayikake – Li et al., 2012, this study; Mushi – Li et al., 2013; Mingyaole – Li et al., 2015a, Li et al., 2015b, this study. (For interpretation of the references to color in this figure legend, the reader is referred to the Web version of this article.)

### 8.2. Regional terrace correlations

Despite spatially varying rates of deformation, the ages on the Mayikake terrace are in general agreement with dated terraces in the western Tarim Basin and along the margins of the Tian Shan: a consistency suggesting a climatic control on the formation of the regional terraces (Fig. 8) (Pan et al., 2003). Nearby terraces at Mushi anticline (Li et al., 2013) and Mingyaole anticline (higher terrace level than in this present study; Li et al., 2015b) have been dated to ~15–19 ka using fine-grain and coarse-grain quartz OSL. Terraces on the flanks of the southern (Hubert-Ferrari et al., 2005) and northern (Thompson et al., 2002; Charreau et al., 2011) Tian Shan date to ~13–18 ka. The deposition of the Mayikake surface dates to ~12–14 ka. These ages (~12–19 ka) suggest the deposition of regionally extensive terrace surfaces during the last deglaciation (MIS 2 to MIS 1) (Fig. 8), followed by rapid subsequent abandonment. Notably, all of these terraces are crossing active structures. Despite the consistent age of regional terrace deposition, the heights of the terraces above the modern rivers vary, suggesting a primarily climatic control on terrace formation, instead of incision due to active tectonics (Pan et al., 2003; Li et al., 2013; Huang et al., 2014).

The age for the Mingyaole terrace (~8–10 ka) does not correlate to other known regional terraces (Fig. 8). Yang and Scuderi (2010) determined a complicated climate history from lakebeds, river terraces, and loess for the Holocene in the western Tarim Basin. Approximately 8 ka, a transition occurred from a drier climate in the early Holocene to a wetter climate during the mid-Holocene, but the records show short-lived periods of arid climate during this interval as well (Yang and Scuderi, 2010). This transition at ~8 ka approximately matches the formation and abandonment of the Mingyaole T2 terrace. Alternatively, the end of deposition on this terrace might be a response to accelerated rock uplift due to outward hinge migration on the southern limb of the growing Mingyaole anticline (Li et al., 2015b).

## 9. Conclusions

We dated deformed fluvial terraces crossing active structures on the NE Pamir margin, northwest China, using OSL and cosmogenic  $^{10}\text{Be}$  dating techniques. Fine-grain (4–11  $\mu\text{m}$ ) quartz OSL samples, when measured using the SMAR protocol, may overestimate the age of a terrace up to a factor of ten. Importantly, we find residual doses still present in both fine and coarse (90–180  $\mu\text{m}$ ) grain sizes on terraces of Late Pleistocene age: ages that can lead to significant overestimation (as much as an order of magnitude) of the terrace age. Thus, dating approaches need to include an adequate assessment of the dose distributions, i.e., small aliquots consisting of few grains and single-grain measurement protocols. Based on the equivalent dose distribution and stratigraphic consistency of ages, we applied the minimum age model (MAM) with a  $\sigma_b$  of 0.1 to the coarse-grain samples to characterize the depositional ages of the terraces. Applying different  $\sigma_b$  values up to 0.4 may increase the OSL MAM ages by 1–10 ka. The cosmogenic depth profiles yielded predictable depth-dependent concentrations for the Mayikake and Mingyaole terraces, with good agreement between the pebble and sand fractions. Cosmogenic  $^{10}\text{Be}$  depth profile ages from three sites date the abandonment of the terrace surfaces to ~8 and ~14 ka. The coarse-grain OSL MAM ages date the deposition of the Mingyaole and Mayikake surfaces to ~9 and ~16 ka, respectively.

Cosmogenic  $^{10}\text{Be}$  and coarse-grain OSL MAM ages agree well. The age of the Mayikake terrace is consistent with other terraces in the western Tarim Basin that date their deposition and subsequent abandonment to the last deglaciation (12–18 ka) (Thompson et al., 2002; Hubert-Ferrari et al., 2005; Li et al., 2012, 2013, 2015b) and suggest the formation of these terraces on the margins of the Tarim Basin and along the flanks of the Tian Shan is climatically controlled (Pan et al., 2003).

Furthermore, new estimated shortening rates of ~3.7, ~4.6, and ~2.4 mm/a on the Mayikake Thrust, Pamir Frontal Thrust, and Mingyaole anticline, respectively, when combined with other published data in the region, suggest temporally uniform shortening across the NE Pamir margin during the Late Quaternary and illuminate the spatial migration of deformation to structures along the Pamir-Tian Shan interface over late Quaternary timescales.

## Acknowledgments

The grant from the US NSF (EAR 1050070), State Key Lab. of Earthquake Dynamics of China (LED2016A05) and the NFSC (41772221) provided funding for this work. Thompson acknowledges support from an NSF Graduate Research Fellowship and an NSF EAPSI fellowship (0914300). This work benefitted from discussion at the 8th New World Luminescence Dating Workshop. We thank Changsheng Wang, Burch Fisher, Zhareen Bulalacao, Yuan Zhaode and Li Wenqiao for help with sample collection and cosmogenic processing and Lauren Simkins and Jon Harvey for valuable discussions in analysis and interpretation. Microsoft Excel spreadsheets provided by Sebastian Hout were greatly appreciated for OSL data analysis. This manuscript was significantly improved by thoughtful comments and suggestions from five anonymous reviewers, B. Guralnik, the editor, and the editor-in-chief.

## Appendix A. Supplementary data

Supplementary data related to this article can be found at <http://dx.doi.org/10.1016/j.quageo.2018.01.002>.

## References

- Aitken, M.J., 1985. *Thermoluminescence Dating*. Academic Press.
- Aitken, M.J., 1998. *Introduction to Optical Dating: the Dating of Quaternary Sediments by the Use of Photon-stimulated Luminescence*. Clarendon Press.

- Anderson, R.S., Repka, J.L., Dick, G.S., 1996. Explicit treatment of inheritance in dating depositional surfaces using in-situ  $^{10}\text{Be}$  and  $^{26}\text{Al}$ . *Geology* 24, 47–51.
- Arnold, L.J., Roberts, R.G., 2009. Stochastic modelling of multi-grain equivalent dose (De) distributions: implications for OSL dating of sediment mixtures. *Quat. Geochronol.* 4, 204–230.
- Bailey, R.M., Arnold, L.J., 2006. Statistical modelling of single grain quartz De distributions and an assessment of procedures for estimating burial dose. *Quat. Sci. Rev.* 25, 2475–2502.
- Balco, G., Stone, J.O., Lifton, N.A., Dunai, T.J., 2008. A complete and easily accessible means of calculating surface exposure ages or erosion rates from  $^{10}\text{Be}$  and  $^{26}\text{Al}$  measurements. *Quat. Geochronol.* 3, 174–195.
- Berger, G.W., 1990. Effectiveness of natural zeroing of the thermoluminescence in sediments. *J. Geophys. Res.* 95 (12), 12375–12397.
- Berger, G.W., Luternauer, J.J., 1987. Preliminary field work for thermoluminescence dating studies at the Fraser River delta, British Columbia. *Geol. Surv. Can. Pap.* 87/IA, 901–904.
- Bookhagen, B., Strecker, M., 2012. Spatiotemporal trends in erosion rates across a pronounced rainfall gradient: examples from the southern Central Andes. *Earth Planet Sci. Lett.* 327, 97–110.
- Borchers, B., Marrero, S., Balco, G., Caffee, M., Goehring, B., Lifton, N., Nishiizumi, K., Phillips, F., Schaefer, J., Stone, J., 2015. Geological calibration of spallation production rates in the CRONUS-Earth project. *Quat. Geochronol.* <https://doi.org/10.1016/j.quageo.2015.01.009>.
- Bøtter-Jensen, L., Bulur, E., Duller, G.A.T., Murray, A.S., 2000. Advances in luminescence instrument systems. *Radiat. Meas.* 32 (5–6), 523–528.
- Bufe, A., Paola, C., Burbank, D.W., 2016. Fluvial beveling of topography controlled by lateral channel mobility and uplift rate. *Nat. Geosci.* <http://dx.doi.org/10.1038/ngeo2773>.
- Bufe, A., Burbank, D.W., Liu, L., Bookhagen, B., Qin, J., Chen, J., Li, T., Thompson Jobe, J.A., Yang, H., 2017. Variations of lateral bedrock erosion rates control planation of uplifting folds in the foreland of the Tian Shan, NW China. *J. Geophys. Res. Earth Surface.* <http://dx.doi.org/10.1002/2016JF004099>.
- Burbank, D.W., Anderson, R.S., 2011. *Tectonic Geomorphology*. John Wiley & Sons.
- Charreau, J., Blard, P.-H., Puchol, N., Avouac, J.-P., Lallier-Verges, E., Bourles, D., Braucher, R., Gallaud, A., Finkel, R., Jolivet, M., Chen, Y., Roy, P., 2011. Pale-erosion rates in Central Asia since 9 Ma: a transient increase at the onset of Quaternary glaciations? *Earth Planet Sci. Lett.* 304, 85–92.
- Chen, J., Burbank, D.W., Schärer, K.M., Sobel, E., Yin, J., Rubin, C., Zhao, R., 2002. Magnetostratigraphy of the upper cenozoic strata in the southwestern Chinese tian shan: rates of Pleistocene folding and thrusting. *Earth Planet Sci. Lett.* 195, 113–130.
- Chen, J., Schärer, K.M., Burbank, D.W., Heermance, R., Wang, C.S., 2005. Quaternary detachment folding of the Mingyaoe anticline, southwestern Tianshan (in Chinese). *Seismol. Geol.* 27, 530–547.
- Chen, Y.G., Lai, K.Y., Lee, Y.H., Suppe, J., Chen, W.S., Lin, Y.N.N., Wang, Y., Hung, J.H., Kuo, Y.T., 2007. Coseismic fold scarps and heir kinematic behavior in the 1999 Chi-Chi earthquake Taiwan. *J. Geophys. Res.* 112, B03S02.
- Chen, H.L., Zhang, F.F., Cheng, X.G., Liao, L., Luo, J.C., Shi, J.B., Wang, J., Yang, C.F., Chen, L.F., 2010. The deformation features and basin-range coupling structure in the northeastern Pamir tectonic belt (in Chinese). *Chinese J. Geology* 45, 102–112.
- Cohen, H., Laronne, J.B., 2005. High rates of sediment transport by flashfloods in the Southern Judean Desert, Israel. *Hydrol. Process.* 19 (8), 1687–1702. <http://dx.doi.org/10.1002/hyp.5630>.
- Colarossi, D., Duller, G.A.T., Roberts, H.M., Tooth, S., Lyons, R., 2015. Comparison of paired quartz OSL and feldspar post-IRSL dose distributions in poorly bleached fluvial sediments from South Africa. *Quat. Geochronol.* 30, 233–238.
- Cunningham, A.C., Wallinga, J., Minderhout, P.S.J., 2011. Expectations of scatter in equivalent dose distributions when using multi-grain aliquots for OSL dating. *Geochronometria* 34 (4), 424–431.
- Cunningham, A.C., Wallinga, J., Hobo, N., Versendaal, A.J., Makaske, B., Middlekoop, H., 2015. Re-evaluating luminescence burial doses and bleaching of fluvial deposits using Bayesian computational statistics. *Earth Surf. Dynam.* 3, 55–65. <http://dx.doi.org/10.5194/esurf-3-55-2015>.
- DeLong, S.B., Arnold, L.J., 2007. Dating alluvial deposits with optically stimulated luminescence, AMS  $^{14}\text{C}$ , and cosmogenic techniques, western Transverse Ranges, California, USA. *Quat. Geochronol.* 2, 129–136.
- Duller, G.A.T., 2003. Distinguishing quartz and feldspar in single grain luminescence measurements. *Radiat. Meas.* 37, 161–165.
- Duller, G.A.T., 2008. Single-grain optical dating of Quaternary sediments: why aliquot size matters in luminescence dating. *Boreas* 37, 589–612.
- Fattahi, M., Nazari, H., Bateman, M.D., Meyer, B., Sébrier, M., Talebian, M., Le Dortz, K., Foroutan, M., Givi, F.A., Ghorashi, M., 2010. Refining the OSL age of the last earthquake on the Dheshir fault, Central Iran. *Quat. Geochronol.* 5 (2), 286–292.
- Fruchter, N., Matmon, A., Avni, Y., Fink, D., 2011. Revealing sediment sources, mixing, and transport during erosional crater evolution in the hyperarid Negev Desert, Israel. *Geomorphology* 134, 363–377.
- Galbraith, R.F., Green, P.F., 1990. Estimating the component ages in a finite mixture. *Nucl. Tracks Radiat. Meas.* 17 (3), 197–206.
- Galbraith, R.F., Roberts, R.G., 2012. Statistical aspects of equivalent dose and error calculation and display in OSL dating: an overview and some recommendations. *Quat. Geochronol.* 11, 1–27.
- Galbraith, R.F., Roberts, R.G., Laslett, G.M., Yoshida, H., Olley, J.M., 1999. Optical dating of single and multiple grains of quartz from Jinmium rock shelter, northern Australia: part 1, experimental design and statistical models. *Archaeometry* 41, 339–364.
- Gosse, J.C., Phillips, F.M., 2001. Terrestrial in situ cosmogenic nuclides: theory and application. *Quat. Sci. Rev.* 20, 1475–1560.
- Gray, H.J., Mahan, S.A., 2014. Variables and potential models for the bleaching of luminescence signals in fluvial environments. *Quat. Int.* <http://dx.doi.org/10.1016/j.quaint.2013.11.007>.
- Guralnik, B., Matmon, A., Avni, Y., Porat, N., Fink, D., 2011. Constraining the evolution of river terraces with integrated OSL and cosmogenic nuclide data. *Quat. Geochronol.* 6, 22–32.
- Haghpor, N., Burg, J.-P., Kober, F., Zeilinger, G., Ivy-Ochs, S., Kubik, P.W., Faridi, M., 2012. Rate of crustal shortening and non-Coulomb behavior of an active accretionary wedge: the folded fluvial terraces in Makran (SE, Iran). *Earth Planet Sci. Lett.* 355–356, 187–198.
- Heermance, R., Chen, J., Burbank, D.W., Miao, J., 2008. Temporal constraints and pulsed Late Cenozoic deformation during structural disruption of the active Kashi foreland, northwest China. *Tectonics* 27, TC6012. <http://dx.doi.org/10.1029/2007TC002226>.
- Heisinger, B., Lal, D., Jull, A.J.T., Kubik, P., Ivy-Ochs, S., Neumaier, S., Knie, K., Lazarev, V., Nolte, E., 2002a. Production of selected cosmogenic radionuclides by muons: 1. Fast muons. *Earth Planet. Sci. Lett.* 200 (3–4), 345–355.
- Heisinger, B., Lal, D., Jull, A.J.T., Kubik, P., Ivy-Ochs, S., Knie, K., Nolte, E., 2002b. Production of selected cosmogenic radionuclides by muons: 2. Capture of negative muons. *Earth Planet. Sci. Lett.* 200 (3–4), 357–369.
- Hetzl, R., Tao, M., Stokes, S., Niedermann, S., Ivy-Ochs, S., Gao, B., Strecker, M.R., Kubik, P.W., 2004. Late Pleistocene/Holocene slip rate of the Zhangye thrust (Qilian Shan, China) and implications for the active growth of the northeastern Tibetan Plateau. *Tectonics* 23, TC6006.
- Hidy, A.J., Gosse, J.C., Pederson, J.L., Mattern, J.P., Finkel, R.C., 2010. A geologically constrained Monte Carlo approach to modeling exposure ages from profiles of cosmogenic nuclides: an example from Lees Ferry, Arizona. *G-cubed* 11. <https://doi.org/10.1029/2010GC003084>.
- Hu, G., Zhang, J.F., Qiu, W.L., Zhou, L.P., 2010. Residual OSL signals in modern fluvial sediments from the Yellow River (HuangHe) and the implications for dating young sediments. *Quat. Geochronol.* 5, 187–193.
- Huang, W.L., Yang, X.P., Li, A., Thompson, J.A., Zhang, L., 2014. Climatically-controlled formation of alluvial platforms and river terraces in a tectonically active region along the southern piedmont of the Tian Shan, NW China. *Geomorphology* 220, 15–29.
- Hubert-Ferrari, A., Suppe, J., Van Der Woerd, J., Wang, X., Lu, H., 2005. Irregular earthquake cycle along the southern Tianshan front, Aksu area, China. *J. Geophys. Res.* 110, B06402. <http://dx.doi.org/10.1029/2003JB002603>.
- Korschinek, G., Bergmaier, A., Faestermann, T., Gerstmann, U.C., Knie, K., Rugel, G., Wallner, A., Dillman, I., Dollinger, G., Liersevon Gostmoski, Ch, Kossert, K., Maiti, M., Poutivest, M., Remmert, A., 2010. A new value for the half-life of  $^{10}\text{Be}$  by Heavy-Ion Elastic Recoil Detection and liquid scintillation counting. *Nucl. Instrum. Meth. Phys. Res. B* 268, 187–191. <http://dx.doi.org/10.1016/j.nimb.2009.09.020>.
- Kreutzer, S., Schmidt, C., Fuchs, M.C., Dietze, M., Fischer, M., Fuchs, M., 2012. Introducing an R package for luminescence dating analysis. *Ancient TL* 30 (1), 1–8.
- Kunz, A., Pflaz, D., Weniger, T., Urban, B., Kruger, F., Chen, Y.-G., 2014. Optically stimulated luminescence dating of young fluvial deposits of the middle Elbe River flood plains using different age models. *Geochronometria* 41, 36–56.
- Lal, D., 1991. Cosmic ray labeling of erosion surfaces: in situ nuclide production rates and erosion models. *Earth Planet Sci. Lett.* 104, 424–439.
- Lee, S.Y., Seong, Y.B., Shin, Y.K., Choi, K.H., Kang, H.C., Choi, J.H., 2011. Cosmogenic  $^{10}\text{Be}$  and OSL dating of fluvial strath terraces along the Osipcheon River, Korea: tectonic implications. *Geosci. J.* 15, 359–378.
- Li, T., Chen, J., Thompson, J.A., Burbank, D.W., Xiao, W., 2012. Equivalency of geologic and geodetic rates in contractional orogens: new insights from the Pamir Frontal Thrust. *Geophys. Res. Lett.* 39, L15305.
- Li, T., Chen, J., Thompson, J.A., Burbank, D.W., Yang, X., 2013. Quantification of three dimensional folding using fluvial terraces: a case study from the Mushi Anticline, northern margin of the Chinese Pamir. *J. Geophys. Res. Solid Earth* 118, 4628–4647. <http://dx.doi.org/10.1002/jgrb.50316>.
- Li, T., Chen, J., Thompson, J.A., Burbank, D.W., Yang, X., 2015a. Active flexural-slip faulting: a study from the Pamir-Tian Shan convergent zone, NW China. *J. Geophys. Res. Solid Earth* 120, 4359–4378. <http://dx.doi.org/10.1002/2014JB011632>.
- Li, T., Chen, J., Thompson, J.A., Burbank, D.W., Yang, H., 2015b. Hinge-migrated fold-scarp model based on an analysis of bed geometry: a study from the Mingyaoe anticline, southern foreland of Chinese Tian Shan. *J. Geophys. Res. Solid Earth* 120, 6592–6613. <http://dx.doi.org/10.1002/2015JB012102>.
- Li, T., Chen, J., Thompson Jobe, J.A., Burbank, D.W., Yang, H., 2017. Active flexural-slip faulting: controls exerted by stratigraphy, geometry, and fold kinematics. *J. Geophys. Res. Solid Earth.* <http://dx.doi.org/10.1002/2017JB013966>.
- Liu, J.F., Chen, J., Yin, J.H., Lu, Y.C., Murray, A., Chen, L.C., Thompson, J., Yang, H.L., 2010. OSL and AMS dating of the Penultimate Earthquake at the Leigu Trench along the Beichuan Fault, Longmen Shan, in the Northeast Margin of the Tibetan Plateau. *Bull. Seismol. Soc. Am.* 100 (5B), 2681–2688.
- Lu, Y.C., Wang, X.L., Wintle, A.G., 2007. A new OSL chronology for dust accumulation in the last 130,000 yr for the Chinese Loess Plateau. *Quat. Res.* 67, 152–160.
- Murray, A.S., Wintle, A.G., 2000. Luminescence dating of quartz using an improved single-aliquot regenerative-dose protocol. *Radiat. Meas.* 32, 57–73.
- Nissen, E., Walker, R.T., Bayasgalan, A., Carter, A., Fattahi, M., Molor, E., Schnabel, C., West, J.A., Xu, S., 2009. The late Quaternary slip-rate of the Har-Us-Nuur fault (Mongolian Altai) from cosmogenic  $^{10}\text{Be}$  and luminescence dating. *Earth Planet Sci. Lett.* 286, 467–478.
- Nishiizumi, K., Imamura, M., Caffee, M.W., Southon, J.R., Finkel, R.C., McAninch, J., 2007. Absolute calibration of  $^{10}\text{Be}$  AMS standards. *Nucl. Instrum. Meth. Phys. Res. B* 258–403.
- Nishiizumi, K., Winterer, E., Kohl, C., Klein, J., Middleton, R., Lal, D., Arnold, J., 1989. Cosmic ray production rates of  $^{26}\text{Al}$  and  $^{10}\text{Be}$  in quartz from glacially polished rocks. *J. Geophys. Res.* 94, 17,907–17,915.
- Olley, J.M., Pietsch, T., Roberts, R.G., 2004. Optical dating of Holocene sediments from a

- variety of geomorphic settings using single grains of quartz. *Geomorphology* 60, 337–358.
- Owen, L.A., Finkel, R.C., Haizhou, M., Barnard, P.M., 2006. Late Quaternary landscape evolution in the Kunlun Mountains and Qaidam Basin, Northern Tibet: a framework for examining the links between glaciation, lake level changes and alluvial fan formation. *Quat. Int.* 154–155, 73–86.
- Owen, L.A., Frankel, K.L., Knott, J.R., Trynhout, S., Finkel, R.C., Dolan, J.F., Lee, J., 2011. Beryllium-10 terrestrial cosmogenic nuclide surface exposure dating of Quaternary landforms in Death Valley. *Geomorphology* 125, 541–557.
- Pan, B., Burbank, D., Wang, Y., Wu, G., Li, J., Guan, Q., 2003. A 900 k.y. record of strath terrace formation during glacial-interglacial transitions in northwest China. *Geology* 31, 957–960.
- Petit, J.R., Jouzel, J., Raynaud, D., Barkov, N.I., Barnola, J.M., Basile, I., Bender, M., Chappellaz, J., Davis, M., Delaygue, G., Delmotte, M., 1999. Climate and atmospheric history of the past 420,000 years from the Vostok ice core, Antarctica. *Nature* 399 (6735), 429–436.
- Porat, N., Duller, G.A.T., Amit, R., Zilberman, E., Enzel, Y., 2009. Recent faulting in the southern Arava, Dead Sea Transform: evidence from single grain luminescence dating. *Quat. Int.* 199, 34–44.
- Porat, N., Zilberman, E., Amit, R., Enzel, Y., 2001. Residual ages of modern sediments in an hyperarid region, Israel. *Quat. Sci. Rev.* 20, 795–798.
- Prescott, J.R., Hutton, J.T., 1994. Cosmic ray contributions to dose rates for luminescence and ESR dating: large depths and long-term time variations. *Radiat. Meas.* 23, 497–500.
- Rees-Jones, J., 1995. Optical dating of young sediments using fine-grain quartz. *Ancient TL* 13, 9–14.
- Repka, J.L., Anderson, R.S., Finkel, R.C., 1997. Cosmogenic dating of fluvial terraces, Fremont River, Utah. *Earth Planet. Sci. Lett.* 152, 59–73.
- Rhodes, E.J., 2011. Optically stimulated luminescence dating of sediments over the past 200,000 years. *Annu. Rev. Earth Planet. Sci.* 39, 461–488.
- Rittenour, T.M., 2008. Luminescence dating of fluvial deposits: applications to geomorphic, palaeoseismic and archaeological research. *Boreas* 37, 613–635.
- Roberts, R.G., Galbraith, R.F., Yoshida, H., Laslett, G.M., Olley, J.M., 2000. Distinguishing dose populations in sediment mixtures: a test of single-grain optical dating procedures using mixtures of laboratory-dosed quartz. *Radiat. Meas.* 32, 459–465.
- Rodnight, H., Duller, G.A.T., Wintle, A.G., Tooth, S., 2006. Assessing the reproducibility and accuracy of optical dating of fluvial deposits. *Quat. Geochronol.* 1, 109–120.
- Sanderson, D.C.W., Bishop, P., Stark, M., Alexander, S., Penny, D., 2007. Luminescence dating of canal sediments from angkor borei, mekong delta, southern Cambodia. *Quat. Geochronol.* 2, 322–329.
- Scharer, K.M., Burbank, D.W., Chen, J., Weldon, R.J., 2006. Kinematic models of fluvial terraces over active detachment folds: constraints on the growth mechanism of the Kashi-Atushi fold system, Chinese Tian Shan. *Geol. Soc. Am. Bull.* 118, 1006–1021. <http://dx.doi.org/10.1130/B25835.1>
- Sobel, E.R., Dumitru, T.A., 1997. Exhumation of the margins of the western Tarim basin during the Himalayan orogeny. *J. Geophys. Res.* 102, 5043–5064. <http://dx.doi.org/10.1029/96JB03267>
- Sobel, E., Chen, J., Schoenbohm, L.M., Thiede, R., Stockli, D.F., Sudo, M., Strecker, M.R., 2013. Oceanic-style subduction controls late Cenozoic deformation of the Northern Pamir orogen. *Earth Planet. Sci. Lett.* 363, 204–218. <http://dx.doi.org/10.1016/j.epsl.2012.12.009>
- Stokes, S., Bray, H.E., Blum, M.D., 2001. Optical resetting in large drainage basins: tests of zeroing assumptions using single-aliquot procedures. *Quat. Sci. Rev.* 20 (5–9), 879–885.
- Stone, J.O., 2000. Air pressure and cosmogenic isotope production. *J. Geophys. Res.* 105 (B10), 23753–23823.
- Thompson, J.A., 2013. Neogene Tectonic Evolution of the NE Pamir Margin. Doctoral Dissertation. UCSB, NW China.
- Thompson, J.A., Burbank, D.W., Li, T., Chen, J., Bookhagen, B., 2015. Late Miocene northward propagation of the northeast Pamir thrust system, northwest China. *Tectonics* 34. <http://dx.doi.org/10.1002/2014TC003690>
- Thompson Jobe, J.A., Li, T., Chen, J., Burbank, D.W., Bufé, A., 2017. Quaternary tectonic evolution of the Pamir-Tian Shan convergence zone, NW China. *Tectonics* 36. <http://dx.doi.org/10.1002/2017TC004541>
- Thompson, S.C., Weldon III, R., Rubin, C.M., Abdрахmatov, K.E., Molnar, P., Berger, G.W., 2002. Late quaternary slip rates across the central Tien Shan, Kyrgyzstan, Central Asia. *J. Geophys. Res. – Solid Earth* 107, 2203.
- Timar-Gabor, A., Wintle, A.G., 2013. On natural and laboratory generated dose response curves for quartz of different grain sizes from Romanian loess. *Quat. Geochronol.* 18, 34–40.
- Trauerstein, M., Lowick, S.E., Preusser, F., Schlunegger, F., 2014. Small aliquot and single grain IRSL and post-IR IRSL dating of fluvial and alluvial sediments from the Pativilca valley, Peru. *Quat. Geochronol.* 22, 163–174.
- Viveen, W., Braucher, R., Bourles, D., School, J.M., Veldkamp, A., van Balen, R.T., Wallinga, J., Fernandez-Mosquera, D., Vidal-Romani, J.R., Sanjurjo-Sanchez, J., 2012. A 0.65 Ma chronology and incision rate assessment of the NW Iberian Mino River terraces based on <sup>10</sup>Be and luminescence dating. *Global Planet. Change* 94–95, 82–100.
- Wallinga, J., 2002. Optically stimulated luminescence dating of fluvial deposits: a review. *Boreas* 31 (4), 303–322. <http://dx.doi.org/10.1111/j.1502-3885.2002.tb01076.x>
- Wang, C., Cheng, X., Chen, H., Ding, W., Lin, X., Wu, L., Li, K., Shi, J., Li, Y., 2016. The effect of foreland palaeo-uplift on deformation mechanism in the Wupoer fold-and-thrust belt, NE Pamir: constraints from analogue modelling. *J. Geodyn.* 100, 115–129.
- Wang, Y., Long, H., Yi, L., Yang, L., Ye, X., Shen, J., 2015. OSL chronology of a sedimentary sequence from the inner-shelf of the East China Sea and its implication on post-glacial deposition history. *Quat. Geochronol.* 30, 282–287.
- Wintle, A.G., Murray, A.S., 2006. A review of quartz optically stimulated luminescence characteristics and their relevance in single-aliquot regeneration dating protocols. *Radiat. Meas.* 41, 369–391.
- Yang, H.L., Chen, J., Porat, N., Li, T., Li, W., Xiao, W., 2017. Coarse- versus fine-grain quartz optical dating of the sediments related to the 1985 Ms7.1 Wuqia Earthquake, northeastern margin of the Pamir salient, China. *Geochronometria* 44, 299–306.
- Yang, X., Scuderi, L.A., 2010. Hydrological and climatic changes in deserts of China since the late Pleistocene. *Quat. Res.* 73, 1–9.
- Zubovich, A.V., Wang, X.Q., Scherba, Y.G., Schelochkov, G.G., Reilinger, R., Reigber, C., Mosienko, O.I., Molnar, P., Michajljow, W., Makarov, V.I., Li, J., Kuzikov, S.I., Herring, T.A., Hamburger, M.W., Hager, B.H., Dang, Y.-M., Bragin, V.D., Beisenbaev, R.T., 2010. GPS velocity field for the Tien Shan and surrounding regions. *Tectonics* 29 (6) TC6014.